XANES evidence for sulphur speciation in Mn-, Ni- and W-bearing silicate melts

Evans, K.A.[*], O'Neill, H. St. C [†], Mavrogenes, J.A.[†], Keller, N.S.[‡], Jang, L-Y [§], Lee, J-F [§]

August 14, 2009

[*]RSES, ANU, ACT 0200, Australia; now at Dept. Applied Geology, Curtin University, GPO Box U1987, Bentley, WA6845, Australia, tel: 0061 8 92664682, fax: 0061 8 92663153, email: k.evans@curtin.edu.au

[†]Research School of Earth Sciences, Building 61, Mills Road, Australian National University, Acton 0200, Australia

[‡]Woods Hole Oceanographic Institution, Clark South 283, MS24, Woods Hole, Ma. 02543

[§]National Synchrotron Radiation Research Centre, 101 Hsin-Ann Road, Hsinchu Science Park, Hsinchu 30076, Taiwan

1 ABSTRACT

S K edge XANES and Mn, W and Ni XANES and EXAFS spectra of silicate glasses synthesised at 1400° C and 1 bar with compositions in the CaO-MgO-Al_2O_3-SiO_2-S plus MnO, NiO, or WO_3 systems were used to investigate sulphur speciation in silicate glasses.

S K-edge spectra comprised a composite peak with an edge between 2470 and 2471.4 eV, which was attributed to S^{2-}, and a peak of variable height with an edge at 2480.2 to 2480.8 eV, which is consistent with the presence of S^{6+}. The latter peak was attributed to sample oxidation during sample storage. W-rich samples produced an additional lower energy peak at 2469.8 eV that is tentatively attributed to the existence of S 3p orbitals hybridised with the W 5d states.

Deconvolution of the composite peak reveals that the composite peak for Mn-bearing samples fits well to a model that combines three Lorentzians at 2473.1, 2474.9 and 2476.2 eV with an arctan edge step. The composite peak for W-bearing samples fits well to the same combination plus an additional Lorentzian at 2469.8 eV. The ratio of the proportions of the signal accounted for by peaks at 2473.1eV and 2476.2eV correlates with Mn:Ca molar ratios, but not with W:Ca ratios. Spectra from Ni-bearing samples were qualitatively similar but S levels were too low to allow robust quantification of peak components. Some part of the signal accounted for by the 2473.1 eV peak was therefore taken to record the formation of Mn-S melt species, while the 2469.8 peak is interpreted to record the formation of W-S melt species. The 2474.9 eV and 2476.2 eV peaks were taken to be dominated by Ca-S and Mg-S interactions. However, a 1:1 relationship between peak components and specific energy transitions is not proposed. This interpretation is consistent with known features of the lower parts of the conduction band in monosulphide minerals and indicates a similarity between sulphur species in the melts and the monosulphides. S XANES spectra cannot be reproduced by a combination of the spectra of the component element monosulphides.

Mn-, W- and Ni- XANES and EXAFS for synthetic glasses without sulphide exsolution did not show any sensitivity to the presence of sulphur, which is unsurprising as S:O ratios were sufficiently low that metals would be mostly co-ordinated by O. Mn EXAFS spectra

were consistent with divalent Mn in 5 co-ordinated Mn-O melt species. W spectra were consistent with tetrahedrally co-ordinated hexavalent W, most likely in scheelite-like melt species, and Ni spectra were consistent with [4] co-ordinated divalent Ni. These results indicate lower coordinations for both W and Ni than those inferred by some previous workers. Cation coordination may reflect the proportion of non-bridging oxygens, which is lower in the Ca-rich and Al-poor samples investigated here than for previous studies.

2 INTRODUCTION

A quantitative understanding of the solubility of sulphur in silicate melts is necessary if we are to understand a wide range of processes that include the distribution of commercially valuable and/or geochemically significant chalcophile elements such as copper, platinum, rhenium, osmium and palladium (e.g. Naldrett, 1999; Wang and Zhou, 2006), the effects of volcanic eruptions on the atmosphere (e.g. de Hoog et al., 2004), global sulphur cycling (e.g. Alt et al., 1993; Fischer et al., 1998), and the formation of magmatic-related economic sulphide deposits (e.g Cawthorn, 2005; Lee and Ripley, 1995; Li and Ripley, 2005; Pina et al., 2006). Quantitative understanding and predictions (e.g. O'Neill and Mavrogenes, 2002; Moretti and Ottonello, 2005) are based on the thermodynamic properties of the melts, which depend on the melt structure, which is a combination of long range structure and the short range combinations of anions and cations that are described as melt species. The term melt species is used here to describe the arrangement of the first coordination shell around the element of interest. Melt structure and speciation have historically proved difficult to identify unambiguously. This is because the temperatures at which silicate melts form are difficult to access with experiments, and because magnified atomic vibrations at high temperature induce significant deviations in the spectroscopic signal so that the results of investigations rarely provide a unique or well constrained solution. Quantification of sulphur speciation is particularly challenging because sulphur can occur in a wide range of oxidation states, from -2 to +6, and because sulphur is a low atomic number element present in low concentrations in silicate melts (less than 1wt%, and often less than 0.1 wt%) which restricts the applicability of many spectroscopic techniques.

Methods used to derive information on the speciation of sulphur in silicate melts include relationships between the concentrations of sulphur and possible ligands such as Fe (O'Neill and Mavrogenes et al., (2002), Mn (Evans et al., 2008), and values of intensive variables such as fO_2 and fS_2 (e.g. Carroll and Rutherford, 1985; Fincham and Richardson, 1954; Wallace and Carmichael, 1992; Carroll and Webster, 1994; O'Neill and Mavrogenes et al., 2002) and the position of the S peak determined by electron microprobe (e.g Carroll and Rutherford,

1988; Metrich and Clocchiati, 1996). These works have shown that sulphur concentrations are highly dependent on melt composition, particularly Fe and Mn (O'Neill and Mavrogenes et al., 2002; Evans et al., 2008), which suggests that S forms melt species with these elements. Ni partition coefficients between silicate melt and olivine (Li et al., 2003) have been used to infer the existence of a Ni-S melt species. Sulphur concentrations are also dependent on the ratio of sulphur to oxygen fugacities, and the form of this relationship indicates that sulphur dissolves as S^{2-} under reducing conditions similar to those found at mid-ocean ridges and as S^{6+} under conditions comparable to those found in the more oxidised arc volcanic environments (e.g. Metrich and Clocchiati, 1996), and that S^{2-} or SO_4^{2-} replace O^{2-} on the anion sublattice (e.g. Fincham and Richardson, 1954).

Further information on the details of sulphur speciation in silicate melts has been provided by XANES (X-ray Absorption Near edge Structure) studies (e.g. Paris et al., 2001; Bonin-Mosbah et al., 2002; Fleet, 2005; Farges et al., 2006; Wilke et al., 2008; Backnaes et al., 2008; Metrich et al., 2009). XANES uses high fluxes of monochromated light from synchrotron light sources to investigate the details of absorption edges of the elements of interest. The spectra consist of measurements of X-ray absorption by a sample as the energy of the X-rays is scanned in small steps from around 100eV below to 100 eV above the absorption edge. Variation in absorption in the vicinity of the edge are created by variation in the probabilities of the different electron transitions as a function of the incoming X-ray energy and by multiple scattering effects. These features are ultimately controlled by the immediate atomic environment of the element of interest, rather than medium or long-range ordering features, and XANES spectra have been used to to determine oxidation state, site geometry, and the identity of nearest neighbours in a wide variety of materials (e.g, Li et al., 1994; Li et al., 1995; Farges et al., 1997; Berry et al., 2006; Liu et al., 2006).

XANES spectroscopy on sulphur-bearing materials of geological interest have been reviewed by Fleet et al. (2005). The sulphur K edge, which is of interest here, is attributed to the transition of S 1s electrons to unoccupied antibonding orbitals at the bottom of the conduction band. The position of the edge changes as a function of sulphur oxidation state, with up to a 12 eV difference between S^{2-} and S^{6+} (e.g. Li et al., 1995), and, to a lesser

extent, as a function of the electronic structure of the lower parts of the conduction bands in the materials examined. Considerable attention has been paid to the XANES spectra of the monosulfides FeS, NiS, CoS, MgS, CaS and MnS (e.g. Farrell and Fleet, 2000; Farrell and Fleet, 2001; Farrell et al., 2002). Results of this work (Fig. 1a) suggest that monosulphides that exhibit a higher degree of covalent bonding, such as FeS and CoS, have a lower energy absorption edge that results from the transition of 1s S electrons into unoccupied S 3p σ^* orbitals hybridised with the metal 3d states. Monosulphides with bonding that has a more ionic character, such as MgS and CaS, have a slightly higher absorption edge energy because the metal 3d states are effectively unavailable for hybridisation in these materials. Spectra for solid solutions between the monosulphide end-members, where accessible, are not linear combinations of the component end-members, which indicates that electronic properties are not a linear function of sample composition. These conclusions are supported by calculated XANES spectra for the monsulphides (Soldatov et al., 2004; Kravtsova et al., 2004).

Most studies of XANES for sulphur-bearing silicate melts have been consistent with the presence of S^{2-} in melts from more reduced settings and S^{6+} in melts from more oxidised environments (e.g Paris et al., 2001; Fleet et al., 2005; Metrich et al., 2009). The presence of tetravalent sulphur has also been proposed on the basis of XANES spectra (Metrich et al., 2002; Bonin-Mosbah et al., 2002), but it has since been demonstrated that, in most cases, this species is an artifact of the intense microbeam used for those measurements (Wilke et al., 2008; Metrich et al., 2009). Spectra for S^{2-}-bearing natural glasses have been found to be similar to linear combinations of the XANES of sulphides of the main cations in the sample, FeS and CaS (Fleet et al., 2005). Formation of CaS_n polyhedral melt species, where n is an unknown stoichiometric coefficient, was also proposed for CaS dissolved in a synthetic sodium aluminosilicate glass (Fleet et al., 2005). Metrich et al. (2009) show qualitatively that the S XANES spectra of synthetic glasses prepared under reducing conditions such that all S is present as S^{2-} are sensitive to the presence or absence of FeO. These observations lead to the hypothesis that S^{2-} in silicate melts is speciated as monosulphide-like melt species of unknown geometry and stoichiometry.

The aim of this study is to use XANES spectra of S in Mn-, Ni- and W-bearing syn-

thetic silicate glasses to investigate the hypothesis that sulphur forms monosulphide-like melt species in silicate melts. These potential ligands were chosen because of their very different effects on sulphur solubility (Evans et al., 2008). Mn strongly enhances sulphur solubility in a similar way to Fe, but has the advantage that its valence is predicted to be 2+ over a wide $f(O)_2$ range, so coupled changes in Mn and S valence during cooling are effectively precluded. Ni at low ppm concentrations causes saturation of the melt with an immiscible NiS phase, and W has little effect on S solubility, which suggests that formation of W-S melt species is limited. Observation of S speciation of melts that contain these three metals should therefore cover a wide range of melt speciation types. XANES and EXAFS (Extended X-ray Absorption Fine Structure) spectra for Mn, Ni and W were also measured to enable a complementary study of the speciation of these metals.

3 METHODS

<begin small type>

3.1 Preparation of synthetic glasses

Preparation methods are described in detail by Evans et al. (2008a). However, brief details are provided here. Sample compositions were based on a CMAS (CaO-MgO-Al_2O_3-SiO_2) anorthite-diopside eutectic mix with added CaO. The Ca was added to increase the base level S concentration in the samples, which reduces analytical uncertainties. This mix is referred to here as CMAS. A number of samples were prepared with zero additive metal content to establish the baseline S XANES for the study. Comparison of these samples allows the repeatability of runs at identical, theoretically, imposed fO_2 and fS_2 values to be assessed. Oxides of Mn, Ni and W were added to the dried oxides and carbonates of Ca, Mg, Al and Si in concentrations that varied from 0.1 wt % to 10 wt%. The exception is run B070406, which contained Ni at 10, 15, 20, 25 and 30 wt %. Sample notation is of the form B$xxxxx$py,

where *xxxxxx* indicates the date of the run, and *y* indicates the sample number from that run.

The glasses were synthesised in vertical muffle tube furnaces which have been modified to allow accurately measured gas mixes to flow upwards through the furnace. All runs were equilibrated at 1400°C. fO_2 and fS_2 were controlled by the proportions of CO, CO_2 and SO_2, which were supplied to the furnace by Tylan F2800 mass flow controllers. Values of fO_2 and fS_2 corresponding to the input gas mixes were calculated as described by O'Neill and Mavrogenes (2002). Uncertainties in fO_2 and fS_2 are estimated to be $\pm$ 0.05 log units (c.f. O'Neill and Mavrogenes, 2002). Samples were run for 24 hours. Previous work (O'Neill and Mavrogenes, 2002) suggests that this time is sufficient for equilibration between the glass and the input gases even when immiscible sulphide melts are formed. After 24 hours the runs were quenched by release of the melt beads into water so quench was close to instantaneous. Such a fast quench should be sufficient to preserve the composition of the melt at 1400°C, with respect to sulphur content, and to preserve melt speciation and structure at the melt-glass transition. However, it is possible that electron exchange continues down to room temperature. Most of the experiments were performed at an fO_2 of -9.6 (ΔQFM=-3.2) and a log fS_2 of -1.91. These conditions have the advantage that they produce high S contents (> 0.2 wt % in most cases) without any risk of blocking the furnace with precipitated elemental S. A small number of experiments were performed at more oxidising conditions but sulphur has previously been shown to be present as S^{2-} in the melt for all the conditions investigated here (O'Neill and Mavrogenes, 2002) except those of B190606 (ΔQFM=3.4). Run conditions for runs that produced data used here are summarised in Table 1.

Glass products were split into portions for electron microprobe and synchrotron analysis. Samples for synchroton analysis were placed into polyethylene containers and stored. The glass beads were kept whole as far as possible, but some disintegrated somewhat during quench and the sample splitting process. Samples for probe analysis were set in EPO-FIX epoxy and polished. These samples were then examined optically for evidence of exsolution of immiscible sulphide and silicate crystal phases. The epoxy-mounted samples were then carbon-coated and analysed for major elements plus S, Mn, W and Ni on the Cameca SX100

electron microprobe at the Research School of Earth Sciences at the Australian National University. WDS analysis and a 15 KeV accelerating voltage was used for all elements. Raw counts were converted to element weight percentages using a modified ZAF correction scheme. The major elements were analysed first using a 10 nA, 15 KeV beam with a 10 micron radius. Sulphur, Mn, W and Ni were subsequently analysed using a 100 nA, 20 micron beam. Details of the sulphur measurement routine, standards, detection limits and uncertainties are provided by Evans et al. (2008a). Time series by O'Neill and Mavrogenes (2002) suggest that the length of experiment utilised here is sufficient for equilibrium to be reached, and the good repeatability of the chemical compositions between runs for this study (Evans et al., 2008) supports this conclusion. However, additional tests for equilibrium were also made in the form of multiple measurements spatially distributed over the glass surface. Samples showing variation in excess of 2% relative to the mean value were discarded.

3.2 XAS analysis

Experimental glass products designated for XANES analysis were dried, where necessary, and stored in glass tubes. The material was taken to the 1.5 GeV NSRRC (National Synchrotron Radiation Research Centre) in Hsinchu, Taiwan, which operates in a 300 mA top-up mode. Sulphur K-edge spectra were measured on BL16A (Dann et al., 1998). This beamline uses a water-cooled Si(111) monochromator to provide monochromated X-rays in the energy range 2000 - 8000 eV. The monochromator energy resolution in the vicinity of S K-edge (2472 eV) is 0.5 eV. Photon flux is a maximum of 3 x 10^{11} photons over an area around 4 x 2 mm. K-edge spectra for Mn, W and Ni were measured on BL17C. This beamline is provided with photons by a wiggler with 20cm period magnets, and energy is monochromated with a Si(111) double crystal monochromator in the range 4 - 15 KeV. Photon flux is 10^{9} to 10^{10} photons per second over an area approximately 8x3mm, and the resolution at the Mn K, Ni K and W L3 edges is around 1 eV.

3.2.1 Sulphur analysis

Glasses and standards were prepared for synchrotron analysis by crushing in an agate mortar under acetone. Crushing was employed to increase sample surface area, expose fresh surfaces for analysis, and decrease the likelihood of data artifacts as a result of self-absorption. Epoxy-mounted samples could not be used for the XANES because of the high S content of epoxy relative to the samples. Calculated absorption lengths, which is the length over which the proportion of penetrating X-ray drops by a factor of e, were 5-7 microns. The crushed material was applied onto S-free kapton tape with a paintbrush. The agate mortar and paintbrush was cleaned thoroughly after each sample was loaded, then re-used. Sample preparation blanks were undertaken by going through all the preparation steps without any sample in the agate mortar. Cl-XANES spectra measured for the sample preparation blanks (Evans et al., 2008b) did not show a signal so cross-contamination between samples is likely to have been negligible. S-XANES was measured for sample-free tape and was found to be free of any sulphur signal. Four samples at a time were loaded onto the sample holder and introduced into the sample chamber. The sample chamber was purged with helium for at least an hour after the sample introduction to remove air introduced during sample loading. The beam upstream of the sample chamber is contained within a helium-filled tube, to minimise X-ray absorption by the air. S K edge spectra were measured in fluorescence geometry, with the sample at 45 degrees to the beam. The fluorescent signal was detected using the in-house Lytle detector. The energy calibration was checked daily with a Mo foil (L3 edge: 2520 eV). Shifts in the monochromator energy were always less than 0.05 eV.

The XANES measurement routine consisted of 1eV, 2 second measurement steps from 2272 to 2442 eV, 0.2 eV, 2 second measurements in the S K edge XANES region from 2442 eV to 2502 eV, and 2 eV, 2 second measurements in the post edge region from 2502 eV to 2847 eV. Passage of the scan over the Cl edge at 2822 eV provided a useful test for contamination from epoxy or other factors as the samples were nominally Cl-free. Scans were repeated three times and averaged to optimise signal quality. Total sample collection time was around three hours for each sample.

Standards investigated included MnS, NiS (millerite), WS_2, $NiSO_4$, $CaSO_4$, $MnSO_4$, FeS and FeS_2. The MnS was sourced from a new container of synthetic MnS from Sigma Aldrich (99% pure). This container was opened for the first time at the beamline on the day of the standard analysis. Millerite and pyrite were taken from natural samples provided by the mineral collection at the Department of Earth and Marine Sciences at the Australian National University. Other standards were taken from the existing chemical collection at the Research School of Earth Sciences, Australian National University. All standards except the MnS were checked with X-ray diffraction prior to the synchrotron experiment. Results were analysed with Siroquant (Taylor, 1991) and contaminants were not detected. It was not possible to measure spectra for CaS and MgS standards because of the extreme tendency of these phases to oxidise on contact with air, which necessitates glove-box facilities for sample insertion. Such facilities were not available at the NSRRC beamline. Instead, spectra were obtained by digitisation of published spectra from Farrell and Fleet (2000). These spectra were aligned with XANES measured for this work by comparison of acquired FeS spectra with digitised FeS spectra from Farrell and Fleet (2000).

The potential for oxidation during sample preparation was investigated because sulphur is susceptible to preparation-induced oxidation (Fleet, 2005). Two subsamples from four of the glass beads were prepared (a) by grinding under acetone in air and (b) by grinding under acetone in a nitrogen-filled glove box. XANES spectra for the two sub-samples were then compared.

3.2.2 Mn, W and Ni analysis

Standards analysed included Mn, Ni, and W metals, MnO, MnO_2, MnS, WS_2, WO_3, $CaWO_4$ (scheelite), NiS (millerite) and NiO. The metal standards were foils provided by the beamline. MnO, MnO_2, MnS and WS_2 were 99% pure or better commercial powders from Sigma-Aldrich. Spectra for the MnO, MnO_2, MnS and WS_2 were taken on the same day that the containers, previously sealed by the manufacturers, were opened. $CaWO_4$ was a natural scheelite; the sample was checked by XRD and found to be >99% pure scheelite. WO_3 and

NiO were >99% pure powders purchased from Sigma-Aldrich. NiS was a natural millerite sample; the identity and purity of the material were confirmed by XRD.

The monochromator energy was calibrated using the metal foils. The first derivative of the Mn K edge, W L3 edge and Ni K edge were set to 6539, 8333 and 10207 eV respectively prior to analysis for each of these metals. All standards except for the pure metals were powdered under acetone in an agate pestle and mortar and applied to kapton tape with a paintbrush. Standard analysis utilised the transmitted signal, to avoid problems with self absorption.

Metal XANES and EXAFS measurements on the samples were performed on either crushed sample applied to tape, as described above for the S K edge measurements, or on the polished sample fragments set in epoxy that were used for the electron microprobe analysis. In the latter case, flexible lead sheet was used to shield the parts of the mount that did not contain the sample under investigation. No systematic difference in sample spectra were noted as a result of the two different sample preparation methods. Sample analysis utilised the fluorescence signal.

Scans across the Mn K-edge were measured for 2 seconds per point in 7 eV steps between 200 and 25eV below the edge, for 2 seconds per point in 0.3 eV steps in the XANES region from 25eV below to 50 eV above the edge, and for 4 seconds per point in 0.06 k unit steps in the EXAFS region from 50 to 540eV above the edge. k is the relative wave number of the photo-electron ejected in the absorption process, and is related to energy by $k^2 = 2m_e(E - E_0)/\hbar^2$, where m_e is the mass of an electron, E and E_0 are the energy and edge energy respectively, and $\hbar$ is the reduced Planck's constant.

Scans across the W L3 edge were measured for 2 seconds per point in 7.5 eV steps between 200 and 20eV below the edge, for 2 seconds per point in 0.4 eV steps in the XANES region from 20eV below to 40 eV above the edge, and for 2 seconds per point in 0.06 k unit steps in the EXAFS region from 80 to 1000eV above the edge.

Scans across the Ni K edge were measured for 2 seconds per point in 10 eV steps between 200 and 20eV below the edge, for 2 seconds per point in 0.4 eV steps in the XANES region

from 20eV below to 80 eV above the edge, and for 4 seconds per point in 0.06 k unit steps in the EXAFS region from 80 to 1000eV above the edge.

3.3 Post Run Analysis and Interpretation

3.3.1 S - XANES

XANES spectra for Mn, W, Ni and S were loaded into the Athena (Ravel and Newville, 2005) software package, which was used for visualisation and manipulation of the data. The multiple spectra from each glass composition were checked for repeatability, averaged, and normalised to an edge step of one, where the edge step was obtained from the difference between a straight line fit to the pre-edge points and a polynomial fit to the the post-edge points extrapolated back to the absorption edge. Spectra for the sulphur standards were corrected for self-absorption using the routine embedded in Athena. The need for self-absorption corrections for the synthetic and natural glasses was assessed using the same routine and was found to be negligible. The position of the main edge was taken to be recorded by the position of the maximum first derivative for each spectra. S K edge spectra were compared with those of the sulphide and sulphate standards as a first order attempt to identify speciation via a fingerprinting approach.

The peak deconvolution facility embedded in Athena was used to quantify the relationships between XANES and sample compositions. Initial fitting attempts were used to refine the number of peaks, peak shape and peak values. Subsequent fits with set peak positions were used to solve for unknown peak areas and widths. The final fitting process utilised, for Mn and Ni bearing samples, Lorentzian peaks centred at 2473.1 eV, 2474.9 eV, 2476.2 eV and, where such a peak was present, at 2481.4 eV. These peaks were superimposed on a arctan function at 2470.8 eV. W-bearing samples required an additional Lorentzian centred at 2469.8 eV, which is subsequently referred to as the W peak. The width of the arctan function was set to 0.3, and the widths and amplitudes of the other peaks were solved for simultaneously by the program. Fits were stable and converged to the same values for a

wide range of starting guesses. The stated uncertainties are propagated from analytical uncertainties based on the noise level of the spectra, and on the goodness of fit. Correlation coefficients were calculated for ratios between peak proportions, normalised to exclude contributions at 2481.4 eV (sulphate signal, see discussion below), and the Ca:additive metal molar ratio.

3.3.2 Mn, W and Ni XANES and EXAFS

XANES for Mn, Ni and W were compared to those of the standards. Particular attention was paid to the Ni pre-edge peak, which as been shown to provide information on Ni coordination (Farges et al., 2001). The pre-edge peak was isolated by a manual spline fit to the main trend of the edge, and the background removed to isolate the pre-edge peak. The centroid of the pre-edge peak was then measured by fit of a Lorentzian peak to the background subtracted XANES spectra. This process was repeated two or three times to assess the sensitivity of results to the manual fitting process. The difference between the centroid energy of the sample and of NiO ($E_{pre-edge,sample}$-$E_{pre-edge,NiO}$) was measured and compared to the calibration of Farges et al., (2001).

The majority of the metal spectra were identical, so the best quality spectra for each metal were averaged, the baseline was subtracted and the signal was transformed into k space, multiplied by k^2 to increase the signal at high k values, and exported into Artemis (Ravel and Newville, 2005). These data were Fourier-transformed and fit to the EXAFS equation (e.g. Fulton et al., 1996). QFS (Quick First Shell) models were adopted for the EXAFS fits; these are appropriate given the probable lack of long range order or structure around the metal-bearing species in the melts. Geometries and initial coordinations for the models were taken from literature sources. Mn models were based on those of McKeown et al. (2003) with octahedrally coordinated oxygens at 2.07 Å. W models were attempted for both octahedrally and tetrahedrally coordinated WO_3 and WO_4^{2-} species respectively, with oxygens at 2.00 Å in the octahedrally coordinated model (Poirier et al., 2005b) and at 1.78 Å in the tetrahedrally co-ordinated model (Hazen et al., 1985). Ni was modelled on

the assumption of formation of octahedral melt species with nearest neighbour oxygens at 2.00 Å; tetrahedral QFS models were also tried and the final results were not sensitive to the initial geometry specification.

The Fourier-transformed spectra were initially fit for four parameters: n, the number of nearest neighbours, E_0, the energy of the edge, σ^2, the mean square relative displacement, which measures the disorder present in the signal, and ΔR, the difference between the starting guess and modelled distance for i-O where i represents the metal of interest. These four parameters control the shape of the Fourier-transformed signal. To a first approximation, peak size increases with n, peak position is related to E_0 and ΔR, and peak breadth increases with σ^2.

The fit value of n can represent an average co-ordination, so, for example, a value of 5 could represent a mixture between tetrahedrally and octahedrally co-ordinated cations with similar bond lengths and comparable melt species geometry. Fits were tried that utilised an additional fit parameter, $c3$, the third cumulant, which measures the asymmetry in the signal disorder, but fits were no better, uncertainties did not decrease, and values of $c3$ were within error of zero. For these reasons the fits documented here used a set $c3$ of zero. Estimates for numbers of nearest neighbours require specification of S_0^2, the passive electron reduction factor, which is multiplied by the number of neighbours in the EXAFS equation (see Fulton et al. (1996) for details). S_0^2 for Mn was taken to be 0.75 (after McKeown et al., 2003), and to be 1 for W and Ni. The value of 1 is probably an overestimate as S_0^2 generally falls between 0.8 and 1, so numbers of nearest neighbours for W and Ni may be underestimated by up to 20%.

The k-range for fitting was taken to run from the first node in the k oscillations outside the XANES region i.e. at around 20-60eV, to the last node before excessive noise destroyed signal quality. This led to k-ranges for the fits from around 3 to around 9 for all Mn, W and Ni. Fits were considered successful when the R-factor for the fit was less than 0.05. The sensitivity of the fit to input parameters such as k-range and k-weighting was also explored and fits that were excessively affected by changes in these parameters were rejected. Uncertainties were taken from the Artemis output and reflect the combination of the effects of statistically

derived uncertainties in the signal and correlations between the fit parameters. Final fits for Ni utilised a set value for the edge energy, which was specified to be the energy at the maximum first derivative of the edge, because correlations between the fit parameters led to a relatively unconstrained solution when the edge energy was allowed to vary freely. The best fit value for the edge energy should not be significantly different to that of the centre of the edge, so this assumption is justified. Fits for Mn and W allowed E_0 to vary and its proximity to the measured edge was used as a complementary measure of fit quality.

<end small type>

4 RESULTS

4.1 Characteristics of synthetic silicate glasses

The appearance and composition of the glasses are described in detail in Evans et al. (2008a). However, essential details are summarised briefly here. Most of the samples formed translucent clear or yellow-coloured glass beads up to 5mm in diameter and 0.05 to 0.15g in weight. A number of samples contained bubbles and/or black specks. In most cases the black specks occurred on the margins of the sample, or showed dendritic form in fractures but appeared to be a surface feature, probably produced on quench, and of insufficient size for analysis. However, in some Ni-bearing samples specks were distributed through the glass and appeared to define flow patterns; probe analysis (Evans et al. 2008a, not shown here) revealed that this apparently exsolved material contained Ni and S with minor Fe. XANES features of these samples are discussed below. Multiple microprobe analysis produced good repeatability in the results for over 90% of the samples analysed, which supports the proposal that equilibrium was attained in most cases. A small number of the glasses produced high totals, up to 102 wt%. These totals are associated with slightly higher Si contents (Table 2), and are therefore attributed to issues with Si analysis which have been noted previously on this machine. Concentrations of other elements such as Mn, W, Ni and S were checked by

comparison against a secondary standard, and shown to be reliable, so the implications and conclusions of this study are unaffected.

Runs without added Mn, W, Ni produced a dissolved S concentration for the CMAS composition of 0.199 ± 0.026 wt % (19 analyses - see Evans et al., 2008 for details). Sulphur content was positively correlated with Mn concentration for the data from the Mn-bearing experiments (Table 2a); sulphur contents were lower at the same Mn content for the more oxidising experimental conditions. S content is effectively independent of W content (Table 2b) and in runs where log fO_2 was increased above -9.6, the S content drops below detection limits for all samples with appreciable W (Evans et al., 2008). Such samples are not discussed here. Ni and S are negatively correlated, with an inverse relationship between S and Ni (Table 2c). This is consistent with equilibration of the melt with a Ni sulphide phase, which was observed to have exsolved from the melt in many of the samples (Evans et al., 2008). Low Fe concentrations are observed in a number of samples. This is attributed to contamination during sample preparation or synthesis. The presence of such low quantities of Fe does not affect the conclusions drawn here.

4.2 Sulphur K-edge XANES

4.2.1 Standards

S K edge XANES for the standards show similar characteristics to those noted in the literature (e.g. Li et al., 1995; Fleet, 2005). Edge energy increases with sulphur oxidation state and with degree of ionicity of bonding at any given oxidation state (Figs 1b,2). The lowest energies are found for FeS and NiS with energies of 2468.7 and 2469 eV respectively. The edge for WS_2, which also contains S as S^{2-}, occurs at slightly higher energy (2470.3 eV), and is coincident with the edge for FeS_2, which contains S^{-}. The edge energy for MnS is 2470.7 eV, significantly higher than for FeS, which is interesting given the similar effects that Mn^{2+} and Fe^{2+} have on S solubility. The non-transition element monosulfides, CaS and MgS, have higher energies again, with edges at 2471.2 and 2471.8 eV respectively. Edge

energy for the sulphates occurs 10-12 eV higher than for the sulphides. The identity of the cation in a sulphate compound has much less effect on the edge energy than for sulphides (Fig. 3), with the edges for $FeSO_4$ and $MnSO_4$ at 2480.2, and that for $NiSO_4$ at 2480.8 eV. The reason for this insensitivity is that O is the nearest neighbour to S in sulphates, so the cation has a much weaker effect on the local electronic enviromnent than it does in the case of the sulphides. Note that tabulated energies (Tables 1 and 2) are edge energies rather than peak energies, which are tabulated in some literature sources (e.g. Li et al., 1995). Edge energies are used here because they are less sensitive to self absorption artifacts than peak energies.

The spectra for NiS, FeS and WS_2 also show a small peak at around 2481eV (Fig. 2). This is in the same position as the sulphate peak, and is attributed to minor standard oxidation during sample storage that was not detected by the pre-run XRD analysis. It is unlikely to be due to oxidation during sample preparation because the MnS standard, which is very prone to oxidation, does not show such features in spite of identical preparation methods.

4.2.2 Synthetic silicate glasses

S K edge spectra for synthetic silicate glasses without sulphide exsolution were significantly different to the spectra of any of the sulphide or sulphate standards (Fig. 4). Well resolved spectra with sufficient information for further quantitative analysis were obtained for samples with S contents greater than 0.18 wt%. Less well resolved spectra with limited information were obtained for samples with S contents between 0.02 and 0.18 wt%.

The main features exhibited by the silicate glass XANES were (1) a composite peak with an edge, for the majority of samples, between 2470 and 2471.5 eV (Fig. 4, Table 2). Mn-, W- and Ni-bearing glasses all produced this peak and its edge energy was not systematically related to sulphur or metal content, or to run conditions. Uncertainties in the edge position, based on measurements of the edge energy from the three spectra for each sample, are of the order of 0.3 eV. Interpretation of the composite peak is discussed further below. Ni-bearing samples from one run, B010806, exhibited edge energies slightly lower than the norm for this

composite peak (Table 2c) but the duplicate of this run, B140906, did not produce the lower edge energies. B010806 samples contained black specks inferred to be exsolved NiS while B140906 did not. However, S contents in the Ni-bearing samples were low, so the spectra are noisy and difficult to interpret unambiguously; (2) a low energy peak at around 2469 eV that was produced only by the W-bearing samples with W contents greater than 1 wt% (runs B141106 and B220806). Run B150906, which contained W contents less than 1 wt %, produced spectra without a discernible 2469 eV peak, referred to hereafter as the W peak; (3) A peak in the same place as that for the sulphate standards with an edge at 2480.8 eV. The size of this peak relative to that of the composite peak was not related in a systematic way to sample composition, preparation methods or experimental run conditions.

4.2.3 Spectral Deconvolution

Good fits (all $\chi^2 < 2$, Table 3, Fig. 5) were obtained for the CMAS, CMAS+Mn, and CMAS+W glasses with sulphur contents greater than 0.18 wt%. It was not possible to obtain unique solutions to the fits for the Ni-bearing glasses because the sulphur contents were low and the signal:noise ratio was too low to uniquely constrain the size of the four peaks. The proportional area of each of the peaks were calculated (Table 3). Two samples with proportional areas for the sulphate peak at 2481.4 eV greater than 20% (B310706p5 and B151106p1) were excluded from further analysis (see discussion) because post-run oxidation is sufficient to have seriously affected the distribution of sulphur species in the sample.

Results (Table 3, Table 4, Fig. 6) showed that there was a good correlation between the proportional areas of the 2473.1 eV peak and the molar Ca:Mn ratio (r=-0.84, Fig. 6a) and between the 2474.9 eV peak and the molar Ca:Mn ratio (r=-0.84, Fig. 6b). These values are significant at the 95% level. Significant correlations were also noted between the Mn concentration and the proportional areas of peaks at 2473.1 eV and 2476.2 eV, and the sulphur concentration and the proportional areas of peaks at 2473.1 eV and 2476.2 eV (Table 4). Mn-bearing glasses from two different runs lie on the same trend. No such correlation was noted between peak proportions and the Ca:W ratio or other compositional parameters

in the W-bearing samples (Fig. 6c, d). The correlation coefficient for the 2473.1 eV peak and the molar Ca:W ratio was -0.43, while that for the 2474.9 eV peak and the molar Ca:W ratio was 0.06. These values are not consistent with a statistically significant correlation. The area of the W peak did not relate systematically to W content, but the peak was poorly resolved so systematic relationships may not have been detectable by this method.

4.3 Mn, W and Ni K-edge XANES and EXAFS

4.3.1 Standards

Standard spectra are consistent with those described in the literature (e.g. McKeown et al. (2003); O'Neill et al., (2008)). MnO (Fig. 7a) shows a pronounced white line and a small pre-edge peak, while MnO_2 shows a larger pre-edge peak but a much less intense white line. The spectra for MnS has a lower edge energy, and lacks any pre-edge peak. W spectra are sensitive to the oxidation state of W, with a lower edge energy for tetravalent W in WS_2, and higher values for hexavalent W in WO_3 and $CaWO_4$. Tetrahedrally co-ordinated W in $CaWO_4$ shows a post-edge bump (Fig. 7b), which is absent in the spectra derived from octahedrally co-ordinated W in WO_3. Ni spectra also show increasing edge energy with increasing oxidation state (Fig. 7c). NiO and NiS spectra are distinctly different, with a pronounced pre-edge peak present in the NiO spectra.

4.3.2 Synthetic silicate glasses

Mn XANES spectra from the glasses resemble that of MnO (Figs 7a and 8a), and the edge position closely matches that of MnO standards measured by McKeown et al. (2003). This implies that Mn is present as the divalent state in the silicate glass. There is no discernible variation in the XANES spectra as a function of Mn:S ratio in the melt (Fig. 8a) or the $\log fO_2/fS_2$ of experiment. The Fourier transform of the EXAFS signal shows a single peak. The shape, location and size of this peak provides information on the nearest neighbours

to Mn in the silicate glass. EXAFS fitting (Fig. 9a) is consistent with Mn surrounded by 5 ± 1 oxygen neighbours at a distance of 2.06 ± 0.02 Å(Table 5). Acceptable fits are not produced for other attempted models. The bond-length is a useful indicator of coordination; McKeown et al. (2003) show that tetrahedral divalent Mn in crystalline silicates and oxides has a Mn-O distance close to 2 $\mathring{A}$, 5 co-ordinated divalent Mn has a Mn-O distance close to 2.15 $\mathring{A}$, and octahedral divalent Mn has a Mn-O distance closer to 2.2 $\mathring{A}$. It is therefore likely that Mn co-ordination is at the lower end of the fit range.

L3 edge XANES spectra for the W-bearing glasses (Fig. 8b) are all very similar to those of O'Neill et al. (2008), who demonstrated from solubility measurements that W dissolves in silicate melts in the 6+ oxidation state at the conditions relevant to this study. The spectra exhibit an intense white line (A) and a post-edge bump (B) before the EXAFS oscillations begin. The post-edge bump is similar but less intense than that shown by tetrahedrally co-ordinated W in Na_2WO_4 (Fig. 7b) and scheelite, $CaWO_4$ (Farges et al., 2006). There is no systematic change in spectra as a function of the oxidation state of the experiment, W:S ratios or absolute W and S contents. Linear combination fitting of the spectra to the two standards using the facility in Athena indicates that a contribution from the tetrahedrally coordinated component alone reproduces the spectra best; addition of an octahedrally coordinated component does not improve the fit. There is no evidence for a WS_2 component. The EXAFS for the W-bearing samples fit well to a model based on a tetrahedral arrangement of four oxygens at 1.75 Å from a central W atom (Table 5, Fig. 9b). EXAFS analysis in which the W-bearing spectra were fit to a WO_3 model, with six oxygens at an average of 2.00 Å distance were unsuccessful. Further attempts in which the oxygens were allowed to vary in distance as described by Poirier et al. (2005b) did not improve the fit quality. These results confirm the suggestion of O'Neill et al. (2008) that W occurs in the 6+ state in silicate melts, and are consistent with the presence of W in the silicate melts investigated here as WO_4 tetrahedra.

Ni K edge XANES spectra for the Ni-bearing glasses are qualitatively similar to those reported by Farges et al. (2001) for divalent Ni in [4], [5] and [6] coordination and superficially resembles that of the NiO standard (Fig. 7c, 8c). The structure is slightly simpler than that

for NiO, however; post-edge complexities are absent in the glass spectra, which is consistent with a resonance cause for the features; a lack of long range structure in the melts will dampen the resonances. There is no systematic change in spectral shape as the Ni:S ratio changes from much greater than 1 in sample B190906p5 to much less than 1, e.g. in sample B231205p5 (Fig. 8c). Nor do the spectra depend on the oxgen and sulphur fugacities at which the glasses formed (not shown).

The difference between centres of the pre-edge peak and that of the NiO standard are 0.4 to 0.6 eV (Table 6). This is consistent with [4] coordinated Ni in the silicate glass according to the calibration of Farges et al. (2001). However, absolute energies of the pre-edge peaks are slightly but systematically different to those recorded by Farges et al. (2001). The pre-edge peaks from this study are centred at 8332.5 to 8332.7 eV, relative to the pre-edge peak of NiO, which is fit by a Lorentzian centred at 8333.15 eV. The results described by Farges et al. (2001) for [4] coordinated glasses are based on peaks centered around energies of around 8330.8 eV relative to NiO at 8331.25 eV. The source of the discrepancy is unclear, as both studies are based on calibration of the Ni metal edge at 8333 eV, and non-linear calibration effects would not be expected to be significant so close to the calibration point.

Fits to the EXAFS yield 3.8 $\pm$ 0.9 nearest neighbour oxygens at 1.96 $\pm$ 0.01$\mathring{A}$ (Table 5, Fig. 9c), which is consistent with the coordination inferred from the pre-edge peak. Other fit parameters (Table 5) are also consistent with results reported by Farges et al. (2001). The possibility that Ni in 4 coordination has oxygens at two distinct Ni-O distances was also investigated but the data was insufficient to distinguish between this model and the single Ni-O distance model, so the simpler model was preferred.

5 DISCUSSION

5.1 Origin of peak at 2481 eV in nominally S^{2-}-bearing glasses

The similarity of the position of the peak at 2481 eV to the main peak in the sulphate standards is consistent with a S^{6+} source for the 2481 eV peak. The peak is therefore referred to subsequently as the sulphate peak. The proportion of the signal associated with this peak, which was obtained from the spectra deconvolution described above, ranged from zero, i.e. the peak was not detectable, to 68% (Table 3). The proportion of the sulphate peak was greater than 5% for six out of the 21 samples for which robust spectral deconvolution was possible (Table 3). The proportion of the sulphate peak was not systematically related to sample sulphur content (Fig. 10a) or the duration of sample storage (Fig. 10b), although the sample with the highest sulphur content, which also had the longest storage time (112 days), had the highest proportion of sulphate peak. The presence of the sulphate peak is a concern, because the experiments were performed in the sulphide stability field so primary sulphate is not expected. However there are a number of unintended causes for the peak that should be considered.

Incorrect gas mixes or inadequate gas flows during the experiment could have resulted in samples more oxidised than intended. However this is an unlikely cause as such factors would have affected all six samples in a run, rather than just one or two, as is the case observed. For example, in run B310706, sulphate peak proportions ranged from to 2% to 68%. Additionally, if sulphate were the stable redox state in the melt then sulphur solubilities would have been far smaller than those measured.

Oxidation during quench is another possibility. It has been shown that S^{6+} can be produced by cooling of natural Fe-bearing S^{2-}-bearing glasses via exchange with the Fe^{2+}-Fe^{3+} redox couple (Metrich et al., 2009). However, all the runs were quenched identically, but only some samples from some runs show oxidation, as discussed for run B310706 above. Additionally, Mn and Ni are unlikely to reduce to a valence less than +2 in order to produce sulphate. W could reduce to a lower valence but the proportion of the sulphate peak in

the W-bearing samples is as low or lower than in the Mn and Ni-bearing samples, so this is unlikely to be a major factor.

Oxidation could have occurred during sample storage. The silicate glasses are highly stressed due to their rapid quenching, and are metastable under room pressure and temperature, and often crumbled to produce a large surface area that would have facilitated reaction subsequent to sample production. The samples were not stored with a dessicant, and the presence of water vapour would have further catalysed sample degradation and sulphate production. This proposal is supported by the higher, though variable, extent of oxidation in samples from run B310706, which was stored for the longest time prior to sample preparation and synchrotron analysis (Fig. 10a).

Sample preparation is known to induce oxidation (e.g. Fleet, 2005) under some circumstances. It is for this reason that four samples were prepared in two ways, with one half of the sample prepared in acetone in air as normal, and the other half prepared in a glovebox filled with nitrogen. There was no systematic increase in the sulphate peak as a result of the preparation protocol. In two cases the nitrogen-prepared portion exhibited a higher sulphate peak (e.g. Fig. 10c), in one the portion prepared under air exhibited the higher sulphate signal (Fig. 10d), and in the final case the two signals were effectively identical (Fig. 4c). It is therefore unlikely that the sample preparation caused the oxidation. These results indicate that oxidised portions of the samples are heterogeneously distributed. A further test of sample preparation was made by preparation of one half of a sample with acetone under air, and the other dry, but again under air. The spectra from these two splits of the same sample were effectively identical. Additionally, preparation of fresh MnS, which is highly susceptible to oxidation, by grinding under acetone did not produce S-XANES spectra with a sulphate peak (Fig. 2). Contamination introduced during sample preparation is also possible. However, this cause is unlikely because the blanks of kapton tape showed no sulphur signal at all, and preparation blanks for Cl-XANES loaded with the same sample protocols (Evans et al., 2008b) showed no cross contamination between samples.

Beam-induced oxidation to produce tetravalent sulphur has also been observed (Wilkes et al., 2008; Metrich et al., 2009) for intense microbeams such as that employed at the ESRF.

606 The beam at the NSRRC is much less powerful, consecutive scans on the same sample do not
607 show any increase in the size of the sulphate peak relative to the composite peak, and there
608 is no peak for tetravalent sulphur. It therefore seems unlikely that the S^{6+} was produced by
609 beam-sample interactions.

610 To summarise, the sporadic nature of the oxidation and the lack of systematic oxidation
611 in any particular run argue against experimental or quench-induced oxidation. Comparison
612 of multiple preparation techniques, repeat analyses, and preparation blanks largely eliminate
613 the possibility that oxidation was caused during sample preparation and analysis. The most
614 likely cause of the oxidation is reaction of the glasses during sample storage. Such oxidation
615 does, in extreme cases, affect the shape of the composite peak (e.g. Fig. 10c,d). For this
616 reason, samples with a sulphate peak proportion greater than 20% were excluded from further
617 analysis. A possible concern is that sulphur oxidation could affect the metal EXAFS results.
618 This is unlikely because metal:S ratios are sufficiently high that even complete oxidation of
619 the sulphur would not significantly change the proportion of metal bonded to the dominant
620 oxygen ligand.

621 ### 5.2 Evidence for tetravalent sulphur

622 Sulphur XANES spectra are consistent with the presence of S^{2-} and S^{6+}. There is no evidence
623 for S^{4+} in the form of an absorption peak between sulphide and sulphate, as proposed by
624 Metrich et al. (2002). This is as expected; Wilke et al. (2008) and Metrich et al., (2009),
625 recently showed that S^{4+} can be produced by the intense photon flux experienced by samples
626 under a synchrotron microbeam. The experiments performed for this study used a mm-size
627 beam and lower photon fluxes than those of Metrich et al. (2002) so beam-induced changes
628 in sample oxidation state were avoided.

5.3 Glass composition effects on the composite peak

The correlations between the proportions of the different components of the composite sulphur peak and the Ca:Mn ratio (Fig. 6a, b) provide evidence that the components of the composite peak relate to melt composition in a systematic way. The simplest interpretation would be that the lowest energy peak (2473.1 eV) is caused by Mn-S interactions in the melt, while the higher energy peaks (2474.9 eV and 2476.2 eV) are related to Mg-S and Ca-S interactions, and the W-peak at 2469.8 eV records W-S interactions.

Such an interpretation would, however, be over simplistic, because (a) the 2473.1 eV peak is not zero in Mn-free samples and (b) the sulphide standard spectra display composite peaks much broader than any of the component peaks found by the deconvolution process, so overlap would be expected to occur between, for example, the Mn:S and Ca:S peak contributions. Peaks in the glass are unlikely to be narrower than those in the sulphides because glasses are much less ordered than crystalline materials, with a consequently broadened XANES signal. It is therefore likely that the deconvolution process is unable to resolve the true complexity of the XANES, and that the four or five peaks that it is possible to resolve, while useful, cannot be assigned on a 1:1 basis to any particular interaction.

A more reasonable proposal is that parts of the signal accounted for by the 2473.1 eV and 2469.8 eV peaks can be attributed to Mn-S and W-S interactions respectively, while parts of the signal accounted for by the 2474.9 eV and 2476.2 eV peaks are caused by Ca-S and Mg-S interactions. Similar results, on qualitative level, were found by Metrich et al. (2009), for CMAS+FeO glass compositions. However, Metrich et al. (2009) only studied Fe-bearing melts with FeO greater than 10 wt%, and so were unable to correlate peak area with metal contents as shown in Fig. 6.

The observations can be explained in terms of the electronic configuration of alkali earth and transition metal sulphides. Transitions to the lowest unoccupied states occur at lower energies for sulphides of the more covalently bonded materials (Mn, W) and at higher energies for sulphides of the more ionically bonded materials (Mg, Ca). For Mn, the transition is likely to be to hybridised S 2p and metal unoccupied 3d orbitals (Farrell et al., 2002), while

for Ca and Mg, the low lying d orbitals are less available for hybridisation which causes the edge energy to increase. The energy of the peak-related transition for a hypothetical W- and S-bearing melt species is harder to determine because the valency of the W is not known and the electronic structure of the conduction band is less well studied. However, the position of a signal from W-S interactions at a lower energy than a signal from Mn-S interactions is consistent with the relative positions of the main edge in the WS_2 and MnS spectra, although the magnitude of the difference is larger for the glass spectra.

Electronic configuration is also related to the conduction properties of the equivalent crystalline sulphides. The more covalent compounds such as MnS and FeS have a smaller band-gap than the compounds with a greater ionic character such as MgS and CaS, and it is the band gap that is reflected by the slightly higher energy of the transition for the alkali earths. However, the peak energies for the glass samples are different to those for the equivalent component sulphides. This is an expected consequence of the different orbital-orbital interactions that occur in a silicate melt where the structure is more relaxed. Less complicated spectra may record the lower signal:noise ratio attainable for the lower S concentrations in the glasses, but may also relate to a lack of mid- to long-range ordering and consequent resonances in the glass structure.

5.4 Features specific to the W-bearing glasses

The low energy peak centred at 2469.8 eV in the S XANES spectra for the CMAS+W melts (e.g. Fig. 4a) is difficult to attribute to a particular transition because the research published on XAS and the electronic configuration of W-S compounds (Dartigeas et al., 1996; Prouzet et al., 2003) is limited and does not address this issue directly. However, the transitions that are most likely to be available to S 1s core electrons in W-S melt species are 3p S $\sigma*$ orbitals hybridised with unoccupied levels in the W 5d orbitals. These orbitals are sparsely occupied in hexavalent tungsten so it is probable that a transition to these orbitals might be energetically favourable compared to the transitions discussed above for CaS and MgS melt species. Regardless of the precise cause of the peak, its existence suggests that S and W do

interact in glasses, contrary to conclusions that would be drawn from studies of S solubility in melts, which indicate that S concentrations in silicate melts are insensitive to W content (Evans et al., 2008). However, the observation cannot be taken as unequivocal evidence for W-S melt species because it is possible that the glass may not faithfully preserve all melt features.

Additional support for the notion that W may form W-S species in melts is provided by consideration of the nature of W bonding in melts. Tungstate species are characterised by a high average bond-valence; four co-ordinated hexavalent tungsten has a bond-valence of 1.5. This means that tungsten is much more likely to attach to network modifiers, because network modifiers, which have lower charge than the network formers Al and Si, can charge balance the high valence W more easily. This observation explains why hexavalent tungsten generally occurs in non-silicate minerals in nature, and the strong dependence of hexavalent tungsten solubility on Ca concentration in melts (O'Neill et al., 2008). It may also indicate that W forms species that combine network modifying cations *and* sulphur. However further work would be required to investigate this possibility.

5.5 Linear combinations of sulphide spectra

Theoretical spectra for mixtures of the standards were calculated to explore the similarity of spectra to those for mixtures of the component sulphides. Mixed spectra were calculated as a molar proportion-weighted sum of the spectra for the individual standards (Fig. 11). Relative weights were taken from expressions for S solubility as a function of metal concentration by O'Neill and Mavrogenes (2002) and Evans et al. (2008a). Validity of the comparison relies on the assumption that the intensity of the S K-α signal is proportional to the S concentration and is not affected by the individual environment of the S. This assumption has been shown to be valid over a range of sulphur contents for metal sulfide solid-solutions (Farrell and Fleet, 2000; 2001; Farrell et al., 2002) and low concentrations of sulphur in coals (Huffman et al., 1991).

XANES spectra of the silicate glasses are not similar to those constructed by linear

combination of spectra from the component sulphides (Fig. 11). This is in contrast to the results of Fleet (2005), who found that XANES of S in synthetic and natural glasses could be produced by a simple combination of the sulphides of the cations present in the samples. The discrepancy might be attributable to (a) lower signal:noise of the Fleet samples, which had lower sulphur contents than those for which results are presented here; or (b) the combination of digitised spectra for CaS and MgS standards from one beamline with measured spectra from another. The CSRF has a resolution of about 0.9 eV at the S K edge (Farrell et al., 2002) and resolution at the NSRRC is around 0.5 eV. Thus features may appear sharper in data from the NSRRC, as shown by a comparison between data for FeS in this work and in Fleet (2005) (not shown). However, there may be other factors that influence the differences between the spectra. Such factors have not been brought to light by the results of this study, and remain mysterious.

5.6 Evidence for formation of metal-S melt species from metal XAS

Mn XANES spectra are very similar to those of Mn-bearing borosilicate waste glasses (McKeown et al., 2003), for which divalent Mn co-ordinated with O was inferred. Mn spectra show no evidence of changes to Mn speciation with increases in S:Mn ratio, and the spectra are consistent with O as the nearest neighbour to divalent Mn. Influences of S in the first coordination shell would be expected to manifest in the form of a reduction in the edge energy and loss of the pre-peak feature at 6540.5 eV. Similarly, spectra from CMAS+Ni and CMAS+W glasses show no evidence for a change in spectral features with changing sulphur content. It should be possible to detect the presence of significant quantities of a Ni-S species because the NiS spectra lacks the pre-edge peak shown by NiO and has a lower edge energy. Expected changes for W would be much less because the W L3 edge is less sensitive to changes in local environment than the K edges for Mn and Ni.

The lack of evidence for formation of metal-S melt species from the metal XAS is, at first sight, contradictory with evidence from the S XAS that supports metal-S interactions. However, the apparent contradiction can be reconciled if the potential proportions of metal-S

and metal-O species are considered. The maximum proportion of the additive metals Mn, W and Ni that could form melt species with sulphur, $p_{\max}$, was calculated from

$$p_{\max} = \frac{n_{\mathrm{S}} - n_{\mathrm{S,CMAS}}}{n_{\mathrm{metal}}} \quad (1)$$

where n_{i} is the number of moles of melt component i per unit mass. $n_{\mathrm{S,CMAS}}$ is the number of moles of S in the end-member CMAS composition. Values could only be calculated reliably for the experiments performed at a $\log_{10} fO_2$ of -9.6 and $\log_{10} fS_2$ of -1.91 as these were the conditions at which the S content of the CMAS composition was best constrained. Values for the Mn-bearing glasses were between 10 and 20%, those for the W-bearing glasses were lower at 1 to 2 %, and those for the Ni-bearing glasses were meaningless, because the loss of the immiscible sulphide phase led to a drop in S content to below the CMAS value.

The absolute maximum ratio of metal:S to metal:O species is therefore 0.2. At this level, the relatively subtle effects on the metal XAS caused by the presence of metal:S species would be difficult to distinguish, as changes in the size of the pre-edge feature of up to 20% are within the uncertainties of the measurement technique. Thus, the metal XAS provides information on the dominant metal complexing agent, which is oxygen, but lesser quantities of metal-S melt species are not precluded.

5.7 Glass composition effects on metal-O coordination

Previous work has inferred that W coordination in silicate melts can be octahedral (Poirier et al., 2005a,b; Farges et al., 2006) or tetrahedral (Farges et al., 2006; O'Neill et al., 2008). EXAFS and XANES results from this work are consistent with dominantly tetrahedrally coordinated W. Work that found octahedral coordination used Si and Al-free melts (Poirier et al., 2005b), whereas the lower coordinations were found for Si- and Al-bearing glasses (Farges et al., 2006). A similar phenomena is noted for the CMAS+Ni melts. Ca-dominated melts are shown by Farges et al. (2001) to contain Ni in [5] or greater coordination whereas this study found pre-edge peaks and EXAFS analysis to indicate somewhat lower coordination of [4] to [5]. A significant difference between the melts in the two studies is the higher Si

and Al content in the CMAS composition, with a significant reduction in the proportion of oxygen that is non-bridging.

A possible explanation for these observations is that a reduction in the availability of non-bridging oxygens, which occurs when a significant proportion of oxygen is involved in the polymeric Si-Al framework of the melt, produces a lower coordination for W and Ni.

6 CONCLUSIONS

Sulphur spectra for CMAS, CMAS+MnO, CMAS+NiO and CMAS+WO_3 are broadly similar, consisting of a broad composite peak plus a variable sulphate signal that is attributed to sulphur oxidation during sample storage. CMAS+W exhibits an additional peak at lower energy that is tentatively attributed to transition between S 1s electrons into a hybridised W 5d - S 3p σ*anti-bonding orbital. There is no evidence for quadravalent sulphur at the low pressures and relatively reduced conditions explored here.

Decomposition of the S K-edge XANES into four component Lorentzian peaks plus an edge step reveals a systematic relationship between peak area and sample composition for the CMAS+Mn melts. Mn:Ca ratios are correlated positively with the proportion of the lower energy peak (2473.1 eV) and negatively with the proportion of the peak at 2474.9 eV. The correlations are significant at the 95% level. Such changes were not noted for the CMAS+W and CMAS+Ni spectra. However, low sulphur contents in CMAS+Ni glasses resulted in low resolution spectra which hinder recognition of changes such as those noted for CMAS+Mn.

Changes in the composite peak shape are consistent with known characteristics of metal-S bonding. Metals that show a greater covalent character in bonding with S, such as Mn, have lower energy hybridised orbitals available, and transitions into these orbitals produce a contribution to the lower energy peak component at 2473.1 eV . Metals that show metal-S bonds with a more ionic character, such as Mg and Ca, have higher energies for the S K-edge because the hybridised orbitals are less available. Thus a large proportion of the signal

accounted for by the 2474.9 eV and 2476.2 eV peaks in the composite peak is attributed to transition of 1s S electrons into S-Ca or S-Mg hybridised orbitals. A 1:1 association between the deconvoluted peaks and the transitions is unlikely because the true complexity of the spectra is likely to have been beyond the resolving power of the deconvolution exercise. Nevertheless, the results provide good evidence for formation of Mn-S and W-S melt species in silicate glasses.

Measured spectra were demonstrated not to be any plausible combination of the component sulphide spectra. The difference between the component sulphide and glass spectra demonstrates that the electronic configuration of S-bearing species in the glasses is quantitatively different to that in the sulphides, although the same processes and elemental properties can be used to provide a qualitative explanation of the observed phenomena.

XANES and EXAFS analysis of Ni, W and Mn can be explained by formation of metal-O melt species and there is no evidence for metal-S bonding, although such evidence would be hard to distinguish, given the low S:O ratio and calculated maximum contributions of metal-S species to the spectra. Mn is likely to be divalent and be coordinated by 4 to 5 oxygens at a distance of 2.06 Å, consistent with the results of previous work. W is likely to be tetrahedrally coordinated with oxygens at a distance of around 1.75 Å, in groups similar to those found in scheelite. Ni EXAFS and pre-edge peak properties are consistent with 4 coordinated Ni-O melt species with Ni-O distances of 1.96 Å. Ni and W both show coordinations lower than those found for previous works that utilised melt compositions with a lower proportion of bridging oxygens. This observation leads to the proposal that metal:O coordination is a function of the ratio of bridging to non-bridging oxygens.

Acknowledgments. Thanks to Dave Clark, Dean Scott and Bob Rapp and staff at the NSRRC, who provided technical input into this project. This work was performed with support from the Australian Synchrotron Research Program (ASRP), which is funded by the Commonwealth of Australia under the Major National Research Facilities Program. Charlie Mandeville and two anonymous reviewers are thanked for perceptive and thought-provoking reviews that improved the paper.

7 REFERENCES

Alt, J. C., Shanks, W. C., and Jackson, M. C. (1993). Cycling of sulfur in subduction zones - the geochemistry of sulfur in the Mariana-island arc and back-arc trough. *Earth. Planet. Sci. Lett.* **119**, 477-494.

Berry, A. J., Hack, A. C., Mavrogenes, J. A., Newville, M., and Sutton, S. R. (2006). A XANES study of Cu speciation in high-temperature brines using synthetic fluid inclusions. *Am. Mineral.* **91**, 1773-1782.

Bonnin-Mosbah, M., Metrich, N., Susini, J., Salome, M., Massare, D., and Menez, B. (2002). Micro X-ray absorption near edge structure at the sulfur and iron K-edges in natural silicate glasses. *Spectrochim. Acta, Part B* **57**, 711-725.

Carroll, M. R. and Rutherford, M. J. (1985). Sulfide and sulfate saturation in hydrous silicate melts. *J. Geophys. Res.* **90**, C601-C612.

Carroll, M. R. and Rutherford, M. J. (1988). Sulfur speciation in hydrous experimental glasses of varying oxidation-state - results from measure wavelength shifts of sulfur X-rays. *Am. Min.* **73**, 845-849.

Carroll, M. R. and Webster, J. D. (1994). Solubilities of sulfur, noble-gases, nitrogen, chlorine, and fluorine in magmas. *Vol. Mag.* **30**, 231-279.

Cawthorn, R. G. (2005). Contrasting sulphide contents of the Bushveld and Sudbury Igneous Complexes. *Min. Dep.* **40**, 1-12.

Dann, T. E., Chung, S. C., Huang, L. J., Juang, J. M., Chen, C. I., and Tsang, K. L. (1998). A high-performance double-crystal monochromator soft X-ray beamline. *J. Synch. Rad.* **5**, 664-666.

Dartigeas, K., Gonbeau, D., and PfisterGuillouzo, G. (1996). Core and valence spectra of TaS2 and WS2 - Experimental and theoretical studies. *J. Chem. Soc., Faraday Trans.* **92**, 4561-4566.

de Hoog, J. C. M., Hattori, K. H., and Hoblitt, R. P. (2004). Oxidized sulfur-rich mafic magma at Mount Pinatubo, Philippines. *Contrib. Mineral. Petrol.* **146**, 750-761.

Evans, K. A., Mavrogenes, J. A., and O'Neill, H. S. J. (2008a). Sulphur solubility and sulphide immiscibility in silicate melts as a function of the concentration of manganese, nickel, tungsten and copper at 1 atmosphere and 1400 C. *Chem. Geol.* **255**, 236-249.

Evans, K. A., Mavrogenes, J. A., O'Neill, H. S., Keller, N. S., and Jang, L. Y. (2008b). A preliminary investigation of chlorine XANES in silicate glasses. *Geochemistry Geophysics Geosystems* **9**.

Farges, F., Brown, G. E., Petit, P. E., and Munoz, M. (2001). Transition elements in water-bearing silicate glasses/melts. Part I. A high-resolution and anharmonic analysis of Ni coordination environments in crystals, glasses, and melts. *Geochim. Cosmochim. Acta* **65**, 1665-1678.

Farges, F., Brown, G. E., and Rehr, J. J. (1997). Ti K-edge XANES studies of Ti coordination and disorder in oxide compounds: Comparison between theory and experiment. *Phys. Rev. B: Condens. Matter* **56**, 1809-1819.

Farges, F., Linnen, R. L., and Brown, G. E. (2006). Redox and speciation of tin in hydrous silicate glasses: A comparison with Nb, Ta, Mo and W. *Can. Mineral.* **44**, 795-810.

Farrell, S. P. and Fleet, M. E. (1999). Evolution of local electronic structure in cubic Mg1-xFexS by SK-edge XANES spectroscopy. *Solid State Commun.* **113**, 69-72.

Farrell, S. P. and Fleet, M. E. (2001). Sulfur K-edge XANES study of local electronic structure in ternary monosulfide solid solution [(Fe, Co, Ni)(0.923)S]. *Phys. Chem. Miner.* **28**, 17-27.

Farrell, S. P., Fleet, M. E., Stekhin, I. E., Kravtsova, A., Soldatov, A. V., and Liu, X. Y. (2002). Evolution of local electronic structure in alabandite and niningerite solid solutions [(Mn,Fe)S, (Mg,Mn)S, (Mg,Fe)S] using sulfur K- and L-edge XANES spectroscopy. *Am. Mineral.* **87**, 1321-1332.

869 Fincham, C. J. B. and Richardson, F. D. (1954). The behaviour of sulphur in silicate and
870 aluminate melts. *Proc. R. Soc. London, Ser. A* **223**, 40-62.

871 Fischer, T. P., Giggenbach, W. F., Sano, Y., and Williams, S. N. (1998). Fluxes and
872 sources of volatiles discharged from Kudryavy, a subduction zone volcano, Kurile Is-
873 lands. *Earth. Planet. Sci. Lett.* **160**, 81-96.

874 Fleet, M. E. (2005). Xanes spectroscopy of sulfur in earth materials. *Can. Mineral.* **43**,
875 1811-1838.

876 Fleet, M. E., Liu, X. Y., Harmer, S. L., and King, P. L. (2005). Sulfur K-edge xanes
877 spectroscopy: Chemical state and content of sulfur in silicate glasses. *Can. Mineral.*
878 **43**, 1605-1618.

879 Fulton, J. L., Pfund, D. M., Wallen, S. L., Newville, M., Stern, E. A., and Ma, Y. (1996).
880 Rubidium ion hydration in ambient and supercritical water. *J. Chem. Phys.* **105**,
881 2161-2166.

882 Hazen, R. M., Finger, L. W., and Mariathasan, J. W. E. (1985). High-pressure crystal-
883 chemistry of scheelite-type tungstates and molybdates. *J. Phys. Chem. Solids* **46**,
884 253-263.

885 Huffman, G. P., Mitra, S., Huggins, F. E., Shah, N., Vaidya, S., and Lu, F. L. (1991).
886 Quantitative-Analysis of All Major Forms of Sulfur in Coal by X-Ray Absorption
887 Fine-Structure Spectroscopy. *Energy Fuels* **5**, 574-581.

888 Kravtsova, A. N., Stekhin, I. E., Soldatov, A. V., Liu, X., and Fleet, M. E. (2004). Elec-
889 tronic structure of MS (M=Ca,Mg,Fe,Mn): X-ray absorption analysis. *Phys. Rev. B:*
890 *Condens. Matter* **69**.

891 Lee, I. S. and Ripley, E. M. (1995). Genesis of Cu-Ni sulfide mineralization in the South
892 Kawishiwi intrusion, Spruce Road area, Duluth complex, Minnesota. *Can. Mineral.*
893 **33**, 723-743.

Li, C., Ripley, E. M., and Mathez, E. A. (2003). The effect of S on the partitioning of Ni between olivine and silicate melt in MORB. *Chem. Geol.* **201**, 295-306.

Li, C. S. and Ripley, E. M. (2005). Empirical equations to predict the sulfur content of mafic magmas at sulfide saturation and applications to magmatic sulfide deposits. *Min. Dep.* **40**, 218-230.

Li, D., Bancroft, G. M., Kasrai, M., Fleet, M. E., Feng, X. H., and Tan, K. (1995). S-K-edge and L-edge X-ray absorption spectroscipy of metal sulfides and sulfates - applications in mineralogy and geochemistry. *Can. Mineral.* **33**, 949-960.

Li, D., Bancroft, G. M., Kasrai, M., Fleet, M. E., Yang, B. X., Feng, X. H., Tan, K., and Peng, M. S. (1994). Sulfur K-edge and L-edge X-ray-absorption spectroscopy of sphalerite, chalcopyrite and stannite. *Phys. Chem. Miner.* **20**, 489-499.

Liu, W., Etschmann, B., Foran, G., Shelley, M., and Brugger, J. (2006). A XANES study of Zn and Fe(II) chloride complexes in hypersaline brines. *Geochim. Cosmochim. Acta* **70**, A364-A364.

McKeown, D. A., Kot, W. K., Gan, H., and Pegg, I. L. (2003). X-ray absorption studies of manganese valence and local environment in borosilicate waste glasses. *J. Non-Cryst. Solids* **328**, 71-89.

Metrich, N., Berry, A. J., O'Neill, H. S. C., and Susini, J. (2009). The oxidation state of sulfur in synthetic and natural glasses determined by X-ray absorption spectroscopy. *Geochim. Cosmochim. Acta* **73**, 2382-2399.

Metrich, N., Bonnin-Mosbah, M., Susini, J., Menez, B., and Galoisy, L. (2002). Presence of sulfite (S-IV) in arc magmas: Implications for volcanic sulfur emissions. *Geophys. Res. Lett.* **29**.

Metrich, N. and Clocchiatti, R. (1996). Sulfur abundance and its speciation in oxidized alkaline melts. *Geochim. Cosmochim. Acta* **60**, 4151-4160.

Moretti, R. and Ottonello, G. (2005). Solubility and speciation of sulfur in silicate melts: The Conjugated Toop-Samis-Flood-Grjotheim (CTSFG) model. *Geochim. Cosmochim. Acta* **69**, 801-823.

Naldrett, A. J. (1999). World-class Ni-Cu-PGE deposits: key factors in their genesis. *Min. Dep.* **34**, 227-240.

Nietubyc, R., Sobczak, E., and Attenkofer, K. E. (2001). X-ray absorption fine structure study of manganese compounds. *J. Alloys Compd.* **328**, 126-131.

O'Neill, H. S. C., Berry, A. J., and Eggins, S. M. (2008). The solubility and oxidation state of tungsten in silicate melts: implications for the comparative chemistry of W and Mo in planetary differentiation processes. *Chem. Geol.* **255**, 346-359.

O'Neill, H. S. C. and Mavrogenes, J. A. (2002). The sulfide capacity and the sulfur content at sulfide saturation of silicate melts at 1400 degrees C and 1 bar. *J. Pet.* **43**, 1049-1087.

Paris, E., Giuli, G., Carroll, M. R., and Davoli, I. (2001). The valence and speciation of sulfur in glasses by X-ray absorption spectroscopy. *Can. Mineral.* **39**, 331-339.

Pina, R., Lunar, R., Ortega, L., Gervilla, F., Alapieti, T., and Martinez, C. (2006). Petrology and geochemistry of mafic-ultramafic fragments from the Aguablanca Ni-Cu ore breccia, southwest Spain. *Econ. Geol.* **101**, 865-881.

Poirier, G., Messaddeq, Y., Ribeiro, S. J. L., and Poulain, M. (2005). Structural study of tungstate fluorophosphate glasses by Raman and X-ray absorption spectroscopy. *J. Solid State Chem.* **178**, 1533-1538.

Poirier, G. L., Cassanjes, F. C., Messaddeq, Y., Ribeiro, S. J. L., Michalowicz, A., and Poulain, M. (2005). Local order around tungsten atoms in tungstate fluorophosphate glasses by X-ray absorption spectroscopy. *J. Non-Cryst. Solids* **351**, 3644-3648.

Prouzet, E., Heising, J., and Kanatzidis, M. G. (2003). Structure of restacked and pillared WS2: An X-ray absorption study. *Chem. Mater.* **15**, 412-418.

945 Ravel, B. and Newville, M. (2005). ATHENA, ARTEMIS, HEPHAESTUS: data analysis
946 for X-ray absorption spectroscopy using IFEFFIT. *J. Synch. Rad.* **12**, 537-541.

947 Soldatov, A. V., Kravtsova, A. N., Fleet, M. E., and Harmer, S. L. (2004). Electronic
948 structure of MeS (Me = Ni, Co, Fe): x-ray absorption analysis. *Journal of Physics-*
949 *Condensed Matter* **16**, 7545-7556.

950 Taylor, J. C. (1991). Computer programs for standardless quantitative analysis of minerals
951 using the full powder diffraction pro?file. *Powder Diffr.* **6**, 2-9.

952 Wallace, P. and Carmichael, I. S. E. (1992). Sulfur in basaltic magmas. *Geochim. Cos-*
953 *mochim. Acta* **56**, 1863-1874.

954 Wang, C. Y. and Zhou, M. F. (2006). Genesis of the Permian Baimazhai magmatic Ni-Cu-
955 (PGE) sulfide deposit, Yunnan, SW China. *Min. Dep.* **41**, 771-783.

956 Wilke, M., Jugo, P. J., Klimm, K., Susini, J., Botcharnikov, R., Kohn, S. C., and Janousch,
957 M. (2008). The origin of S^{4+} detected in silicate glasses by XANES. *Am. Mineral.* **93**,
958 235-240.

TABLES

Table 1: Summary of run conditions

Run	Additive metal	Additive conc (wt%)	$\mathrm{Log}_{10}\ fO_2$	$\mathrm{Log}_{10}\ fS_2$	$\mathrm{Log}_{10}\ fSO_2$	ΔQFM
B030106	Mn	1-10	-9.60	-1.91	-3.06	-3.2
B310706	Mn	1-10	-9.60	-1.91	-3.06	-3.2
B020806	Mn	1-10	-7.18	-0.84	-0.61	-0.7
B111006	Mn	0-1	-7.59	-2.80	-1.50	-1.2
B151106	Mn	0-1	-9.60	-1.91	-3.06	-3.2
B301205	W	0-1	-9.60	-1.91	-3.06	-3.2
B240306	W	1-10	-9.60	-1.91	-3.06	-3.2
B220806	W	1-10	-9.60	-1.91	-3.06	-3.2
B230806	W	1-10	-7.18	-1.85	-0.61	-0.7
B150906	W	0-1	-9.60	-1.91	-3.06	-3.2
B200906	W	1.5-10	-3.09	-10.85	-0.52	3.3
B141106	W	1-10	-9.60	-1.91	-3.06	-3.2
B231205	Ni	0-1	-9.60	-1.91	-3.06	-3.2
B220306	Ni	1-10	-9.60	-1.91	-3.06	-3.2
B070406	Ni	10-30	-9.60	-1.91	-3.06	-3.2
B120406	Ni	1-10	-7.18	-1.85	-0.61	-0.7
B010806	Ni	0-1	-9.60	-1.91	-3.06	-3.2
B030806	Ni	0-1	-7.18	-1.85	-0.61	-0.7
B140906	Ni	0-1	-9.60	-1.91	-3.06	-3.2
B190906	Ni	1-10	-3.09	-11.88	-1.52	3.3

Table 2a: Electron microprobe analyses of Mn-bearing samples

Sample	Si(wt%)	Al(wt%)	Mg(wt%)	Ca(wt %)	Fe(wt%)	S(wt%)	Mn(wt%)	O(wt%)	Total(wt%)	Edge (eV)
B030106p2 ‡	19.93(8)	6.64(4)	5.07(3)	24.54(5)	0.73(1)	0.224(1)	0.381(3)	42.31(1)	99.9(2)	n.a.
B310706p1 *	20.3(1)	6.98(6)	5.43(5)	25.32(9)	0.018(1)	0.196(3)	bdl	43.2(2)	101.5(5)	2471.3
B310706p2 *	19.5(1)	6.91(2)	5.35(7)	24.91(1)	0.04(2)	0.332(3)	2.07(2)	42.8(1)	102.0(2)	2470.4
B310706p3 *	18.9(2)	6.58(9)	5.17(7)	24.2(2)	0.043(9)	0.480(2)	3.74(5)	42.0(4)	101.1(8)	2470.5
B310706p4 *	18.4(1)	6.44(2)	5.06(2)	23.71(7)	0.05(1)	0.726(6)	6.03(2)	42.0(1)	102.4(2)	2470.4
B310706p5	18.2(1)	6.3(1)	4.87(7)	23.24(7)	0.07(3)	0.879(4)	7.15(2)	41.8(1)	102.5(3)	2470.6
B310706p6 *	17.6(2)	6.10(9)	4.76(7)	22.36(6)	0.06(2)	1.117(8)	8.74(3)	41.2(2)	102.0(4)	2470.9
B020806p1	17.6(2)	6.19(3)	4.75(1)	22.62(5)	bdl	0.088(3)	9.008(1)	40.5(2)	100.8(4)	2470.8
B020806p2 *	18.40(5)	6.39(2)	4.993(3)	23.76(8)	0.02(2)	0.053(2)	6.10(3)	41.25(9)	101.0(2)	2471.4
B020806p3 *	17.93(5)	6.3(1)	4.92(8)	23.29(3)	0.040(7)	0.12(1)	7.27(2)	40.8(2)	100.7(3)	2470.5
B020806p4	19.4(1)	6.76(5)	5.29(9)	25.07(8)	bdl	0.024(2)	2.122(7)	42.3(2)	101.0(3)	2470.5
B020806p5	19.12(5)	6.69(4)	5.09(8)	24.62(6)	bdl	0.039(2)	3.902(7)	42.10(5)	101.6(1)	2471
B020806p6 ‡	18.1(1)	6.3(1)	4.87(7)	23.3(1)	bdl	0.122(4)	7.24(2)	41.0(2)	101.0(4)	2471.2
B111006p2	20.2(5)	7.6(7)	4.9(8)	24.(1)	bdl	0.019(7)	1.02(9)	43.0(3)	101.2(2)	n.a.
B151106p1	21.08(9)	7.08(4)	5.25(2)	22.03(7)	0.048(7)	0.229(2)	0.379(5)	42.93(9)	99.1(1)	2471.2
B151106p4	20.84(5)	6.95(6)	5.20(2)	21.93(6)	0.05(2)	0.274(5)	1.070(6)	42.7(1)	99.2(2)	2471.4
B151106p5	21.19(4)	7.02(7)	5.22(6)	22.02(6)	0.096(8)	0.219(7)	0.235(3)	42.94(4)	99.0(1)	2471.2
B151106p6	20.89(7)	6.95(3)	5.18(6)	21.82(6)	0.065(4)	0.251(4)	0.840(7)	42.62(9)	98.7(1)	2471.5

*: S XANES depicted

‡: Mn XANES depicted

n.a.: not available

Table 2b: Electron microprobe analyses of W-bearing samples

Sample	Si(wt%)	Al(wt%)	Mg(wt%)	Ca(wt %)	Fe(wt%)	S(wt%)	W(wt%)	O(wt%)	Total(wt%)	Edge (eV)
B301205p3 ‡	19.8(1)	6.65(6)	5.15(5)	24.38(2)	0.486(7)	0.208(2)	0.740(6)	42.1(2)	99.6(3)	n.a.
B240306p1	20.60(6)	7.32(6)	5.55(1)	15.53(3)	0.06(1)	0.075(4)	7.74(4)	41.97(9)	98.9(2)	n.a.
B220806p2	21.59(1)	7.63(9)	5.80(5)	16.03(5)	0.048(1)	0.064(4)	5.86(4)	43.23(1)	100.3(2)	2469
B220806p3	21.1(1)	7.39(7)	5.69(5)	15.50(7)	0.05(1)	0.068(7)	7.6(1)	42.6(1)	100.0(3)	2468.8
B220806p4	23.08(5)	8.14(5)	6.14(7)	16.77(2)	0.020(7)	bdl	2.23(3)	44.92(9)	101.4(2)	n.a.
B220806p5	22.8(2)	7.89(3)	6.09(6)	19.73(2)	0.06(2)	0.073(5)	0.223(7)	45.0(2)	101.9(4)	2469
B220806p6	20.51(9)	7.32(7)	5.6(1)	15.1(2)	0.05(1)	0.071(3)	9.27(5)	42.1(2)	100.1(6)	2470.6
B230806p5 ‡	22.8(2)	8.00(8)	6.2(1)	16.6(1)	bdl	bdl	2.34(4)	44.4(4)	100.3(9)	n.a.
B200906p5 ‡	19.2(1)	6.61(8)	5.31(7)	24.46(4)	bdl	bdl	2.67(4)	41.7(1)	100.0(3)	n.a.
B150906p1	19.7(2)	7.0(3)	5.5(5)	25.1(3)	bdl	0.3(1)	0.70(9)	42.9(2)	101.4(4)	2471.1
B150906p2	20.1(1)	6.93(6)	5.36(6)	25.1(1)	0.040(5)	0.200(3)	0.28(3)	42.9(2)	101.0(4)	2471.2
B150906p3	19.7(1)	6.83(5)	5.39(9)	24.95(7)	0.18(2)	0.206(4)	0.89(3)	42.5(2)	100.7(3)	2471.4
B150906p4	19.9(1)	6.89(6)	5.4(1)	25.14(9)	0.17(2)	0.202(5)	0.49(5)	42.7(2)	101.0(3)	2471.2
B150906p5	21.16(3)	7.32(1)	5.80(8)	22.80(9)	0.163(7)	0.134(2)	bdl	43.7(1)	101.1(3)	2471.4
B141106p1 *	18.4(3)	6.6(2)	5.16(5)	22.0(3)	0.07(2)	0.14(2)	6.4(2)	40.9(7)	100.(2)	2468.9
B141106p2 *	19.5(2)	6.8(4)	5.2(3)	24.8(8)	bdl	0.10(2)	2.4(2)	42.1(6)	101.(1)	2469.0
B141106p3	20.2(7)	6.7(4)	5.1(8)	23.5(8)	0.01(2)	0.05(4)	3.8(1)	42.7(6)	102.(2)	2469.5
B141106p4	17.57(8)	6.22(4)	5.27(5)	20.55(9)	0.05(3)	0.18(5)	10.1(4)	40.1(2)	100.0(6)	2470.6

*: S XANES depicted

‡: W XANES depicted

n.a.: not available

Table 2c: Electron microprobe analyses of Ni-bearing samples

Sample	Si(wt%)	Al(wt%)	Mg(wt%)	Ca(wt %)	Fe(wt%)	S(wt%)	Ni(wt%)	O(wt%)	Total(wt%)	Edge (eV)
B231205p1 ‡	19.81(8)	6.64(2)	5.14(3)	24.96(2)	0.374(7)	0.214(2)	0.016(2)	42.2(1)	99.3(2)	n.a.
B231205p5	19.8(2)	6.74(5)	5.15(7)	24.82(3)	0.521(4)	0.214(2)	bdl	42.3(2)	99.5(4)	n.a.
B220306p3	19.5(1)	7.22(9)	5.5(1)	24.63(3)	0.10(1)	0.188(5)	0.021(3)	42.3(3)	99.5(7)	n.a.
B070406p6	22.717(8)	8.46(6)	6.5(1)	16.89(8)	0.04(2)	0.058(5)	0.033(2)	44.50(6)	99.2(2)	n.a.
B120406p6 ‡	18.7(9)	6.9(3)	5.3(2)	24.6(2)	0.02(2)	0.022(3)	0.312(9)	41.(1)	97.(3)	n.a.
B010806p1 *	20.04(8)	7.00(9)	5.50(5)	25.80(9)	0.04(1)	0.180(4)	0.016(4)	43.2(1)	101.8(3)	2470.5
B010806p2	23.73(4)	8.28(4)	6.47(7)	17.26(3)	0.03(1)	bdl	0.132(8)	45.64(7)	101.7(1)	n.d.
B010806p4	23.6(1)	7.9(2)	6.4(2)	17.37(9)	0.018(7)	bdl	0.091(4)	45.2(2)	100.7(4)	2469
B010806p5	20.1(1)	7.02(1)	5.47(7)	25.53(9)	0.032(9)	0.021(9)	0.10(4)	43.1(2)	101.5(4)	2468.5
B030806p2	20.2(1)	7.04(1)	5.4(1)	25.71(5)	0.05(2)	0.021(8)	0.38(4)	43.2(3)	101.9(6)	n.a.
B030806p5	20.0(1)	6.98(9)	5.4(2)	25.3(2)	0.02(2)	0.016(2)	0.354(5)	42.7(4)	100.7(9)	n.a.
B140906p4 *	20.2(1)	6.96(7)	5.3(1)	25.68(6)	0.08(1)	0.203(3)	0.025(6)	43.2(2)	101.6(5)	2471.2
B140906p5	20.18(9)	7.00(2)	5.28(6)	25.641(8)	0.104(7)	0.199(3)	bdl	43.16(8)	101.6(1)	2471.2
B190906p5	19.8(1)	6.84(8)	5.40(4)	24.1(1)	0.020(5)	bdl	2.473(7)	42.4(2)	101.0(4)	n.a.

*: S XANES depicted
‡: Ni XANES depicted
n.a.: not available

Table 3: Results of S XANES deconvolution

Sample	Additive	Additive metal (wt %)	S (wt %)	Metal:Ca (molar)	Storage (Days)	P(W)	P(2473.1))	P(2474.9)	P(2476.2)	P(2481.4)	χ^2
B310706p1	Mn	0	0.196	0.0000	113	n.a.	0.11(3)	0.34(7)	0.36(5)	0.19(2)	1.548
B310706p2	Mn	2.07	0.332	0.0606	113	n.a.	0.33(3)	0.21(5)	0.44(4)	0.020(6)	0.355
B310706p3	Mn	3.74	0.48	0.1127	113	n.a.	0.26(3)	0.26(6)	0.36(4)	0.11(1)	0.396
B310706p4	Mn	6.03	0.726	0.1855	113	n.a.	0.31(3)	0.19(4)	0.44(4)	0.06(1)	1.553
B310706p6	Mn	8.74	1.117	0.2852	113	n.a.	0.03(4)	0.22(7)	0.06(4)	0.68(6)	1.124
B151106p1	Mn	0.379	0.229	0.0126	16	n.a.	0.10(3)	0.22(6)	0.27(5)	0.41(5)	0.283
B151106p1N	Mn	0.378	0.229	0.0125	16	n.a.	0.13(4)	0.45(10)	0.40(7)	0.02(1)	0.284
B151106p4	Mn	1.07	0.274	0.0356	16	n.a.	0.19(4)	0.40(9)	0.41(6)	n.a.	0.289
B151106p5	Mn	0.235	0.219	0.0078	15	n.a.	0.15(4)	0.43(9)	0.40(6)	0.03(1)	0.261
B151106p6	Mn	0.84	0.251	0.0281	16	n.a.	0.16(4)	0.44(10)	0.40(7)	n.a.	0.24
B150906p1	W	0.7	0.3	0.0203	70	n.a.	0.14(4)	0.36(9)	0.45(7)	0.05(2)	0.784
B150906p2	W	0.28	0.2	0.0081	70	n.a.	0.15(3)	0.38(8)	0.47(6)	n.a.	1.865
B150906p3	W	0.89	0.206	0.0260	71	n.a.	0.17(4)	0.34(8)	0.46(6)	0.04(1)	0.636
B150906p4	W	0.49	0.202	0.0142	71	n.a.	0.22(3)	0.25(6)	0.52(6)	0.01(2)	1.536
B150906p5	W	0	0.134	0.0000	71	n.a.	0.16(3)	0.34(8)	0.49(6)	n.a.	0.742
B141106p1	W	6.4	0.14	0.0634	11	0.07(1)	0.11(4)	0.3(1)	0.49(8)	n.a.	1.401
B141106p2a	W	2.4	0.1	0.0211	11	0.09(1)	0.13(3)	0.24(7)	0.46(6)	0.09(2)	0.588
B141106p2b	W	2.4	0.1	0.0223	11	0.08(1)	0.07(3)	0.32(9)	0.43(8)	0.10(2)	0.952
B140906p4	Ni	0.03	0.203	0.0008	71	n.a.	0.15(3)	0.38(8)	0.47(6)	n.a.	0.639
B140906p4D	Ni	0.03	0.203	0.0008	71	n.a.	0.29(3)	0.18(5)	0.53(5)	n.a.	0.693
B140906p5	Ni	0.03	0.199	0.0008	71	n.a.	0.21(3)	0.33(7)	0.46(5)	0.001(4)	1.494

n.s.: not significant

P(xxxx) indicates the proportion of the signal accounted for by the peak at xxxx eV

Table 4: Correlation coefficients between peak areas and sample composition for Mn-bearing samples

	Mn	Ca	S	Mn:Ca
	wt %	wt %	wt %	molar
P(2473.1)	0.85	n.s.	0.8	0.84
P(2474.9)	-0.85	n.s.	-0.81	-0.84
P(2476.2)	n.s.	n.s.	n.s.	n.s.

P(xxxx) indicates the proportion of the signal accounted for by the peak at xxxx eV

Table 5: Results of EXAFS fitting. Table headings defined in section 3.3

	n	E_0	r(Å)	σ^2	R factor
Mn	5(1)	6540(4)	2.06(2)	0.009(3)	0.007
W	3(1)	10204(3)	1.77(1)	0.001(1)	0.023
Ni	3.8(9)	8345*	1.96(1)	0.007(4)	0.036

*: Energy set to maximum first derivative on edge

Table 6: Ni pre-edge peak centroid energies

Sample	$E_{pre-edge,sample}$-$E_{pre-edge,NiO}$ (eV)	1 σ (eV)
B231205p1	0.48	0.07
B220306p6	0.49	0.05
B120406p6	0.56	0.05
B070406p6	0.41	0.16
B190906p5	0.49	0.04
B030806p5	0.5	0.04
B030806p2	0.45	0.05
NiO	0	n.a.

8 FIGURE CAPTIONS

Figure 1: a: Schematic comparison of the transitions that result in the sulphur K edge for compounds with a greater ionic bonding character, such as MgS, and those with a greater covalent bonding character, such as FeS; b: Summary of edge positions, defined as the maximum first derivative, versus oxidation state for standards measured in this study.

Figure 2. S K edge XANES spectra for sulphide standards. Peak at 2481eV indicated by the dotted line is spurious sulphate caused by oxidation of the samples prior to sample preparation and analysis. Spectra for CaS and MgS are digitised from Farrell and Fleet (2000). All other spectra were measured at the NSRRC.

Figure 3. S K edge XANES spectra for sulphate standards. All spectra were measured at the NSRRC.

Figure 4. S K edge XANES spectra for selected synthetic silicate glasses. Peak at 2481eV is spurious sulphate caused by oxidation of the samples prior to sample preparation and analysis. a: Effect of changes in additive metal on XANES for CMAS (sample B310706p1), CMAS+Ni (sample B010806p1), CMAS+Mn (sample B310706p2), CMAS + W (samples B141106p1). b: Effect of changes in additive metal content on XANES for CMAS+Mn compositions for B310706p3 (3.7 wt% Mn), B310706p4 (6.0 wt% Mn) and B310706p6 (8.7 wt% Mn); c: Effect of changes in sample preparation method for sample B140906p4. See also Fig. 10c,d; d: Effect of oxidation state of experiment on S K edge XANES spectra for, from the top down, B020806p2, B310706p6, B020806p3, B310706p2. Both experiments were performed in the sulphide stability field. Samples chosen to illustrate the range of sulphate signal produced by samples from within the same run.

Figure 5. Example of results of S XANES peak deconvolution exercise. Thicker line is the measured XANES. Thin lines are the deconvoluted peak components and fit XANES. a: B310706p1 (CMAS); b: B310706p4 (CMAS+Mn); c: B141106p2b (CMAS+W).

Figure 6. Results of S XANES peak deconvolution exercise. Spectra with proportion of signal accounted for by the 2481.4 eV (sulphate-related peak) greater than 0.2 and with low signal:noise are omitted. a: Relationship between the proportion of the signal accounted for by the peak at 2473.1 eV and the molar Mn:Ca ratio; b: Relationship between the proportion of the signal accounted for by the peak at 2474.9 eV and molar Mn:Ca ratio; c: Relationship between the proportion of the signal accounted for by the peak at 2473.1 eV and W:Ca ratio; d: Relationship between the proportion of the signal accounted for by the peak at 2476.9 eV and W:Ca ratio.

Figure 7. Metal XANES spectra for the metal standards. a: Mn standards; b: W standards; c: Ni standards. All metal standards were measured on BL17C at the NSRRC.

Figure 8. Metal XANES spectra for the synthetic glasses. a: Mn K edge spectra in order of decreasing Mn:S ratio; b: W L3 edge spectra in order of decreasing W:S ratio. A indicates the intense white line, B indicates the post-edge feature discussed in the text; c: Ni K edge spectra in order of decreasing Ni:S ratio.

Figure 9. Results of metal EXAFS fitting. R is distance in Angstroms. $|\chi(R)|$ is the magnitude of the Fourier-transformed signal as a function of R. The shape, position and size of the peak provides information on the nearest neighbours to the metal probed by the EXAFS measurements. Solid line is data, dashed line is the fit. a: average of Mn-bearing glasses. b: Average of W-bearing glasses; c: average of Ni-bearing glasses.

Figure 10. Further information on the sullphate peak at 2481.4 eV. a: relationship between sample storage duration and the proportion of the signal accounted for by the 2481.4 eV peak; b: relationship between sample sulphur content and the proportion of the signal accounted for by the 2481.4 eV peak; c: comparison of XANES for the two portions of B140906p1 prepared under air and in a nitrogen-filled glovebox. The extension N indicates preparation in the glovebox; d: comparison of XANES for the two portions of B151106p1 prepared under air and in a nitrogen-filled glovebox. The extension N indicates preparation in the glovebox. Dashed line indicates position of sulphate peak.

1018 Figure 11. Comparison of S K edge XANES spectra with sums of sulphide spectra for a:
1019 B310706p1 (CMAS); b: B310706p6 (CMAS+Mn); c: B141106p1 (CMAS+W).

9 FIGURES

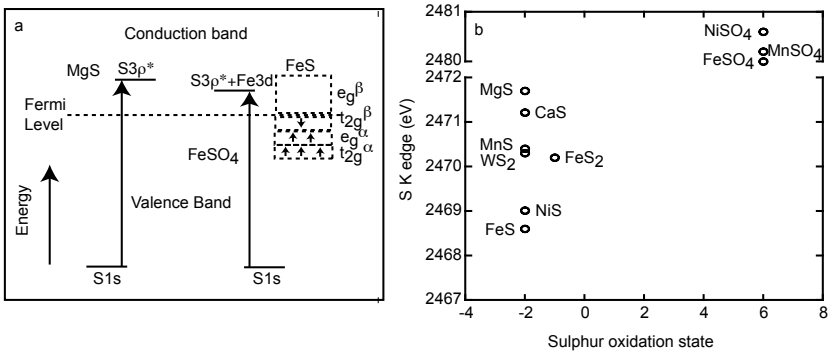
a
Conduction band
MgS
S3ρ*
S3ρ*+Fe3d
FeS
Fermi
Level
FeSO4
Energy
Valence Band
S1s
S1s
b
NiSO4
MnSO4
FeSO4
MgS
CaS
MnS
WS2
FeS2
NiS
FeS
S K edge (eV)
Sulphur oxidation state

Figure 1:

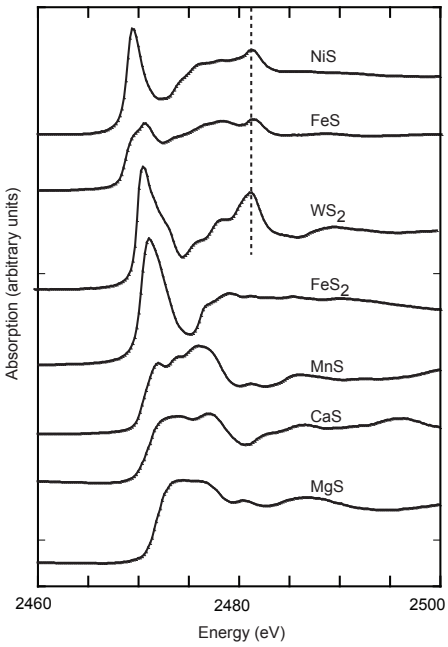
NiS
FeS
WS2
FeS2
MnS
CaS
MgS
Absorption (arbitrary units)
2460
2480
2500
Energy (eV)

Figure 2:

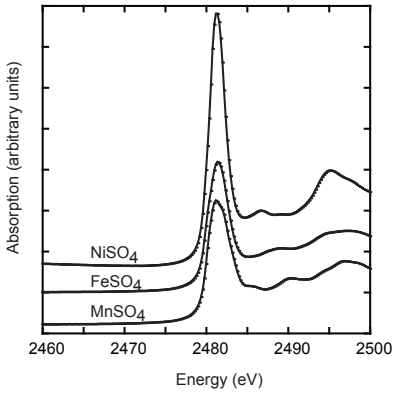
Absorption (arbitrary units)
NiSO4
FeSO4
MnSO4
2460
2470
2480
2490
2500
Energy (eV)

Figure 3:

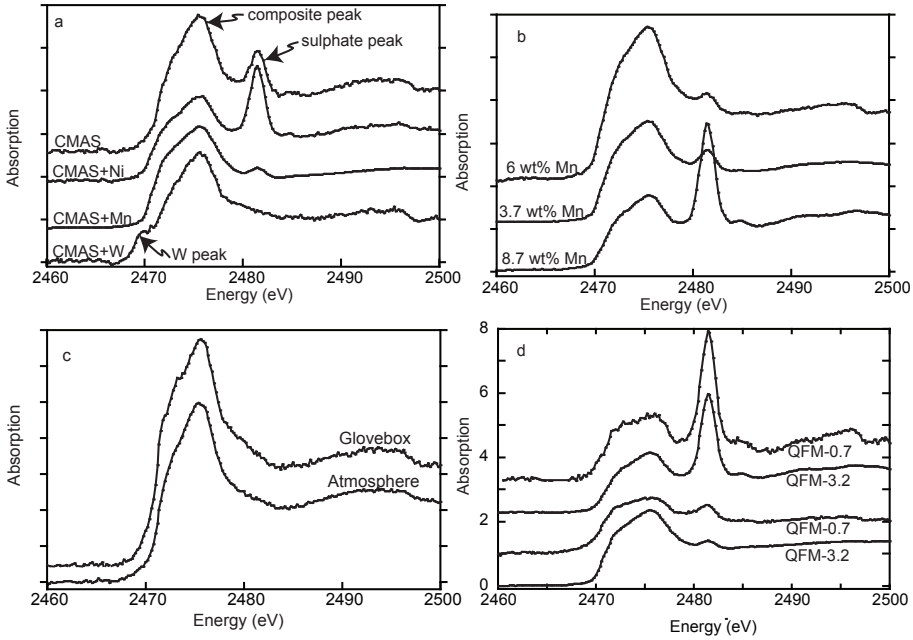
a
composite peak
sulphate peak
CMAS
CMAS+Ni
CMAS+Mn
CMAS+W
W peak
Absorption
Energy (eV)
b
6 wt% Mn
3.7 wt% Mn
8.7 wt% Mn
c
Glovebox
Atmosphere
d
QFM-0.7
QFM-3.2
QFM-0.7
QFM-3.2

Figure 4:

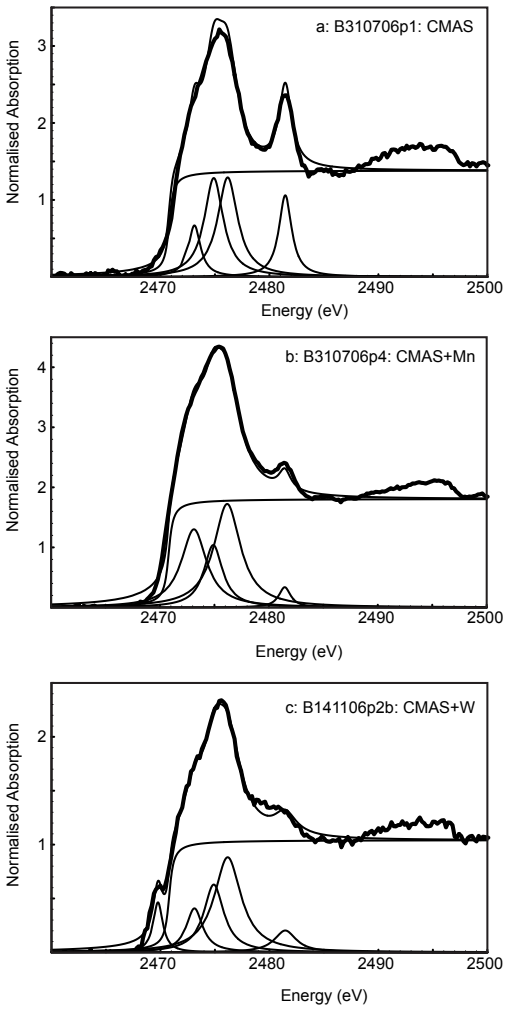
a: B310706p1: CMAS
Normalised Absorption
Energy (eV)
b: B310706p4: CMAS+Mn
Normalised Absorption
Energy (eV)
c: B141106p2b: CMAS+W
Normalised Absorption
Energy (eV)

Figure 5:

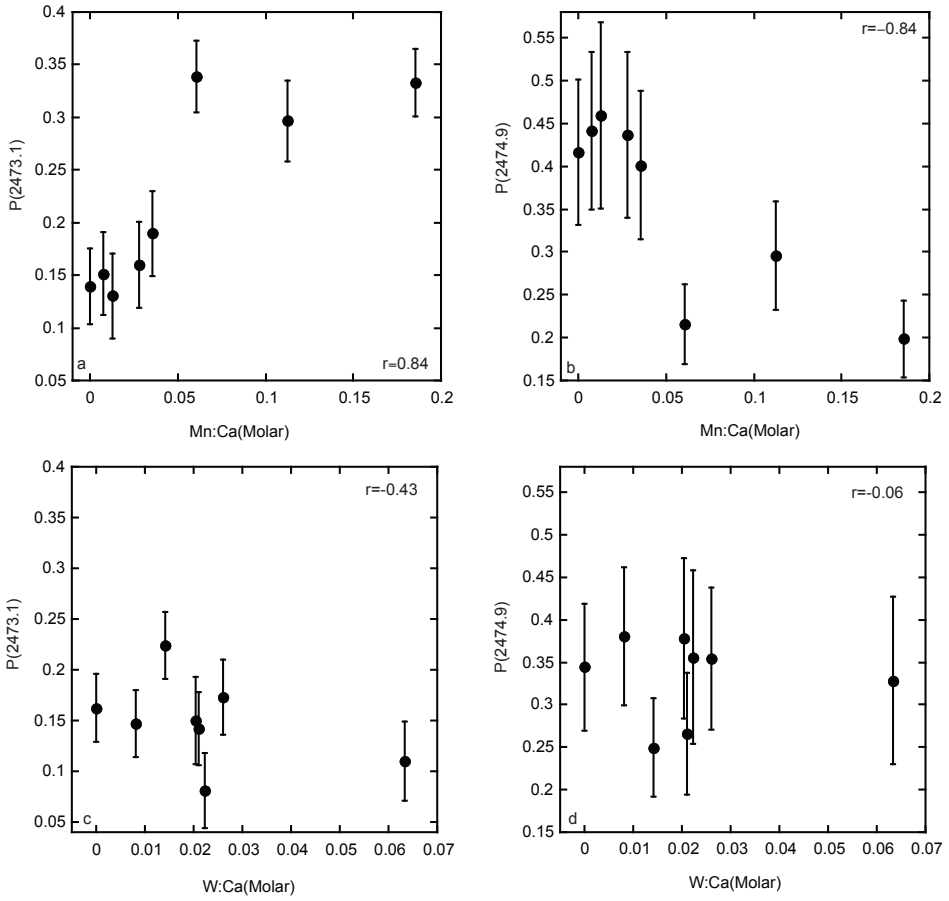

Figure 6:

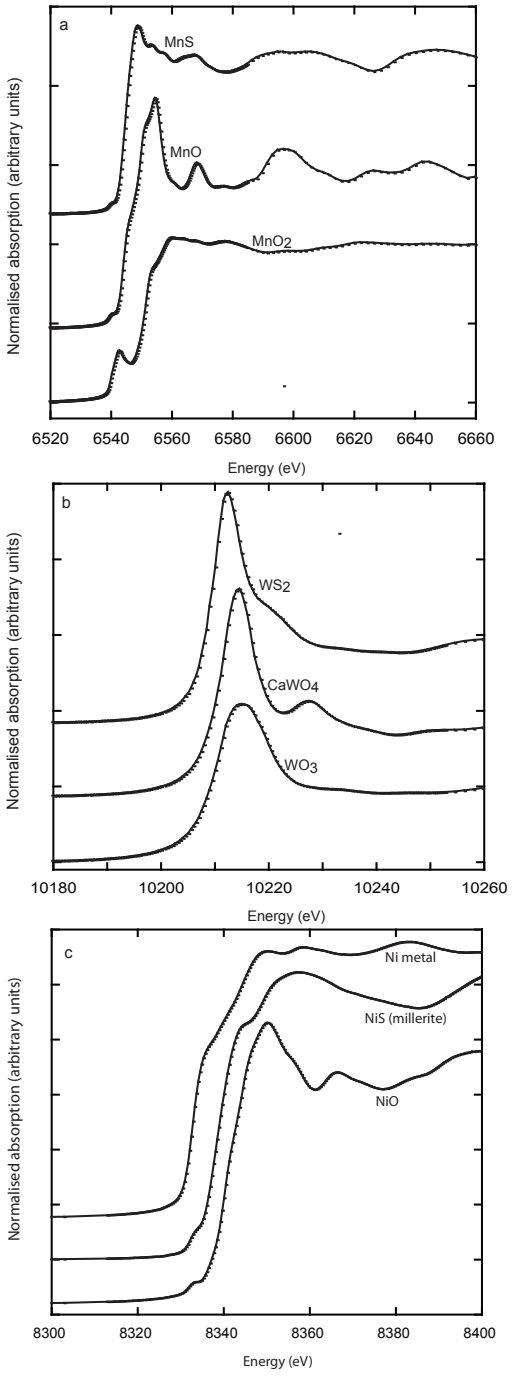
a
MnS
MnO
MnO2
Normalised absorption (arbitrary units)
6520
6540
6560
6580
6600
6620
6640
6660
Energy (eV)
b
WS2
CaWO4
WO3
Normalised absorption (arbitrary units)
10180
10200
10220
10240
10260
Energy (eV)
c
Ni metal
NiS (millerite)
NiO
Normalised absorption (arbitrary units)
8300
8320
8340
8360
8380
8400
Energy (eV)

Figure 7:

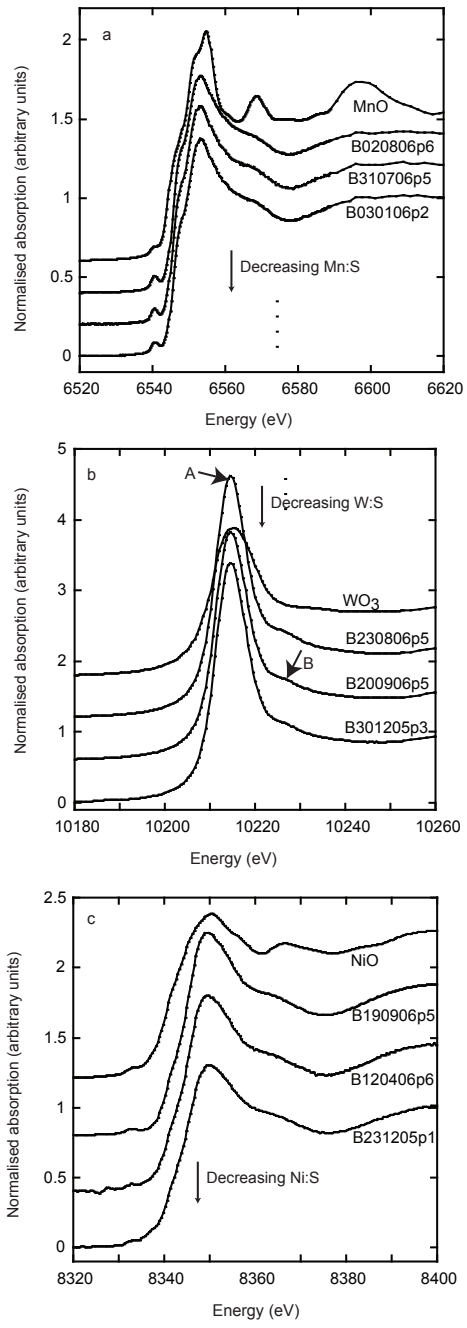
a
MnO
B020806p6
B310706p5
B030106p2
Decreasing Mn:S
Normalised absorption (arbitrary units)
Energy (eV)
b
A
B
Decreasing W:S
WO3
B230806p5
B200906p5
B301205p3
Normalised absorption (arbitrary units)
Energy (eV)
c
NiO
B190906p5
B120406p6
B231205p1
Decreasing Ni:S
Normalised absorption (arbitrary units)
Energy (eV)

Figure 8:

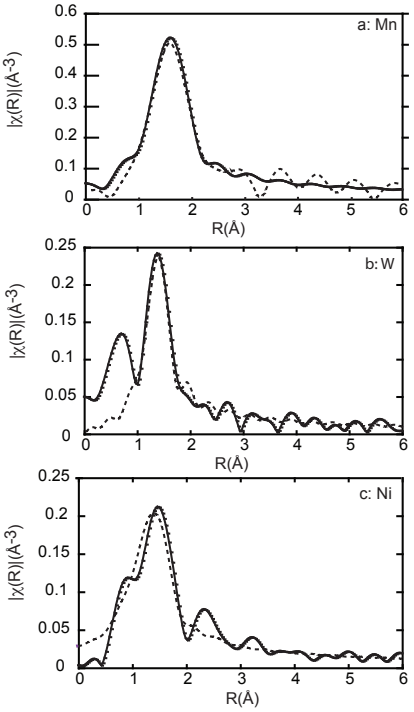

Figure 9:

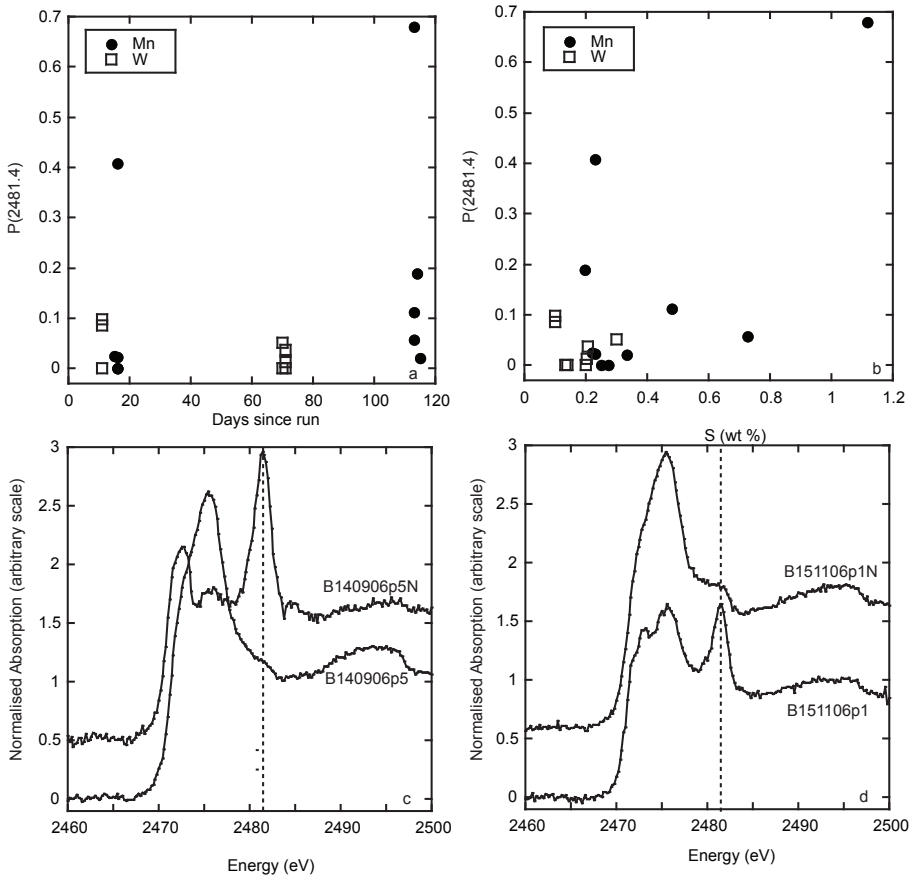
Mn
W
P(2481.4)
Days since run
a
b
S (wt %)
Normalised Absorption (arbitrary scale)
B140906p5N
B140906p5
B151106p1N
B151106p1
Energy (eV)
c
d

Figure 10:

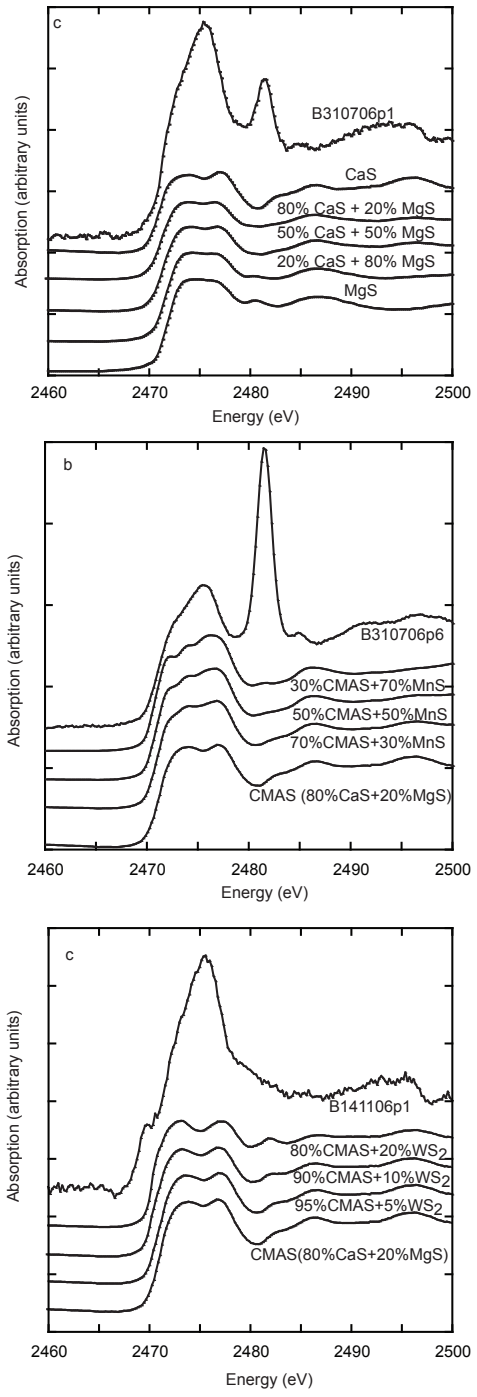
c
B310706p1
CaS
80% CaS + 20% MgS
50% CaS + 50% MgS
20% CaS + 80% MgS
MgS
Absorption (arbitrary units)
2460
2470
2480
2490
2500
Energy (eV)
b
B310706p6
30%CMAS+70%MnS
50%CMAS+50%MnS
70%CMAS+30%MnS
CMAS (80%CaS+20%MgS)
Absorption (arbitrary units)
2460
2470
2480
2490
2500
Energy (eV)
c
B141106p1
80%CMAS+20%WS2
90%CMAS+10%WS2
95%CMAS+5%WS2
CMAS(80%CaS+20%MgS)
Absorption (arbitrary units)
2460
2470
2480
2490
2500
Energy (eV)

Figure 11: